

**FIRST-PRINCIPLES CRYSTAL STRUCTURE PREDICTION:
A METHOD DEVELOPMENT
AND ITS APPLICATION TO HYDROGEN STORAGE MATERIALS**

M.Sc. THESIS

Engin AYBEY

Department of Computational Science and Engineering

Computational Science and Engineering Programme

MAY 2014

**FIRST-PRINCIPLES CRYSTAL STRUCTURE PREDICTION:
A METHOD DEVELOPMENT
AND ITS APPLICATION TO HYDROGEN STORAGE MATERIALS**

M.Sc. THESIS

**Engin AYBEY
(702111002)**

Department of Computational Science and Engineering

Computational Science and Engineering Programme

Thesis Advisor: Doç. Dr. Adem Tekin

MAY 2014

**AB INITIO KRİSTAL YAPI TAHMİNİ:
METOT GELİŞTİRME
VE HİDROJEN DEPOLAMA MALZEMELERİNE UYGULANMASI**

YÜKSEK LİSANS TEZİ

**Engin AYBEY
(702111002)**

Hesaplamalı Bilim ve Mühendislik Anabilim Dalı

Hesaplamalı Bilim ve Mühendislik Programı

Tez Danışmanı: Doç. Dr. Adem Tekin

MAYIS 2014

To my dear parents and elder sister,

FOREWORD

This thesis is submitted in candidacy for the M.Sc. degree from the Istanbul Technical University (ITU). Firstly, I would like to extend my sincerest thanks to Assoc. Prof. Dr. Adem Tekin for his great help, supervision, patience and friendship. Secondly, I would like to extend my gratitude to Informatics Institute of ITU for supplying the computer cluster, MARS, which was used for all computations in this thesis.

Finally, I would like to express my heartfelt thanks to my parents and elder sister for their love and support.

May 2014

Engin AYBEY
(M.Sc. Student)

TABLE OF CONTENTS

	<u>Page</u>
FOREWORD	ix
TABLE OF CONTENTS	xi
ABBREVIATIONS	xiii
LIST OF TABLES	xv
LIST OF FIGURES	xvii
SUMMARY	xxi
ÖZET	xxiii
1. INTRODUCTION	1
2. HYDROGEN STORAGE	3
2.1 Importance of Hydrogen Storage	3
2.2 Hydrogen Storage Methods	4
3. CRYSTAL STRUCTURE PREDICTION	9
3.1 Crystal Structure Prediction Algorithms	9
3.1.1 USPEX	9
3.1.2 CALYPSO	9
3.1.3 XtalOpt	10
3.1.4 GASP	10
3.1.5 CASPESA.....	10
4. COMPUTATIONAL BACKGROUND	13
4.1 Simulated Annealing	13
4.1.1 Method.....	14
4.2 Density Functional Theory	18
4.2.1 The Schrödinger equation.....	18
4.2.2 Electron density	19
4.2.3 Thomas-Fermi model	20
4.2.4 The Hohenberg-Kohn theorems	20
4.2.5 The Kohn-Sham approach	22
4.3 The Improved CASPESA.....	24
4.3.1 SA setup.....	28
4.3.1.1 $Mn(BH_4)_2$	28
4.3.1.2 $LiMg(BH_4)_3(NH_3)_2$	29
4.3.2 DFT setup	30
5. RESULTS AND DISCUSSIONS	33
5.1 $Mn(BH_4)_2$	33
5.2 $LiMg(BH_4)_3(NH_3)_2$	40
6. CONCLUSIONS	51
REFERENCES	55

CURRICULUM VITAE..... 61

ABBREVIATIONS

CSP	: Crystal Structure Prediction
SA	: Simulated Annealing
DFT	: Density Functional Theory
CASPESA	: CrystAl Structure PrEdiction via Simulated Annealing
USPEX	: Universal Structure Predictor, Evolutionary Xtallography
CALYPSO	: Crystal structure AnaLYsis by Particle Swarm Optimization
GASP	: Genetic algorithm for Structure Prediction
HK	: Hohenberg-Kohn
LDA	: Local Density Approximation
GGA	: Generalized Gradient Approximation

LIST OF TABLES

	<u>Page</u>
Table 5.1 : The minimum bond lengths of $Mn(BH_4)_2$ structures shown in Figures 5.1a and 5.1b, respectively. Here, vc (variable-cell) represents the DFT geometry optimization of the structure with the relaxations of internal atomic coordinates and lattice parameters.	33
Table 5.2 : The minimum bond lengths and energies of $Mn(BH_4)_2$ structures (for which variable-cell (vc) optimizations were carried out) shown in Figures 5.3a and 5.5a, respectively.	37
Table 5.3 : The progress of the improved CASPESA method for $Mn(BH_4)_2$. It shows how the bond constraints, cost function and energy of $Mn(BH_4)_2$ were readjusted along the iterations of the method. Bold ones indicate the lowest energy in each iteration.	39
Table 5.4 : The cell parameters, crystal symmetries and energies of the $Mn(BH_4)_2$ structures considered in this study.	39
Table 5.5 : Comparison of bond thresholds and cost function boundary in the experimental (Figure 5.8a) and relaxed (Figure 5.8b) structures.....	41
Table 5.6 : The progress of the improved CASPESA method with using <i>set</i> 1 for $LiMg(BH_4)_3(NH_3)_2$. It shows how the bond constraints, cost function and energy of $LiMg(BH_4)_3(NH_3)_2$ were readjusted along the iterations of the method. Bold ones indicate the lowest energy in each iteration.....	42
Table 5.7 : The minimum bond and total energies of structures shown in Figure 5.10.....	43
Table 5.8 : Comparison of bond length constraints in the experimental and the structures found with the improved CASPESA method using <i>set</i> 1 and <i>set</i> 2. Total energies (in eV) for two formula units were obtained from the variable-cell DFT calculations.....	45
Table 5.9 : The progress of the improved CASPESA method with using <i>set</i> 2 for $LiMg(BH_4)_3(NH_3)_2$. It shows how the bond constraints, cost function and energy of $LiMg(BH_4)_3(NH_3)_2$ were readjusted along the iterations of the method. Bold ones indicate the lowest energy in each iteration.....	45
Table 5.10 : The total energies and minimum bond distances of the structures in Figure 5.12.....	46

Table 5.11: Cell parameters and energies (eV) of the $LiMg(BH_4)_3(NH_3)_2$ structures found with the improved CASPESA using set 1 and set 2 in addition to the experimental structure [16]...... 47

LIST OF FIGURES

	<u>Page</u>
Figure 2.1 : Hydrogen cycle: water dissociation by electrolysis while the oxygen is released to the atmosphere, hydrogen storage and finally combustion of hydrogen with oxygen from the atmosphere in a fuel cell or internal combustion engine. The product of the combustion is only water [18].....	4
Figure 2.2 : Fossil fuel reserves-to-production (R/P) ratios at end 2012 [19].	4
Figure 2.3 : The six basic hydrogen storage methods and phenomena. The gravimetric density ρ_m , the volumetric density ρ_v , the working temperature T, and pressure p are listed. RT stands for room temperature (25°C) [20].	5
Figure 2.4 : Volumetric and gravimetric hydrogen density graphs of metal hydrides and DOE targets. a) Volumetric and gravimetric hydrogen density of some hydrides. $LiBH_4$ exhibits the highest gravimetric hydrogen density of 18 mass%. [20] b) Revised United States Department of Energy(DOE) targets for hydrogen storage [21].	6
Figure 4.1 : Flowchart of SA Algorithm [55].	14
Figure 4.2 : Flowchart of the improved CASPESA method.....	27
Figure 4.3 : CASPESA model of $Mn(BH_4)_2$ [10]. Representation of colors; green: manganese (Mn), pink: boron (B), white: hydrogen (H).	28
Figure 4.4 : CASPESA model of $LiMg(BH_4)_3(NH_3)_2$. Representation of colors; purple: lithium (Li), green: magnesium (Mg), blue: nitrogen (N), pink: boron (B), white: hydrogen (H).....	29
Figure 5.1 : The experimental and its relaxed structures of $Mn(BH_4)_2$. a) The experimental trigonal $Mn(BH_4)_2$ [15] structure with $P3_112$ (IT: 151) symmetry. b) The variable-cell DFT optimized of the experimental $Mn(BH_4)_2$ [15]. (number of formula units of (a) and (b) in the unitcell,Z=9). IT represents the crystal symmetry numbers based on international tables for crystallography. Representation of colors; purple: manganese (Mn), green: boron (B), white: hydrogen (H).	33
Figure 5.2 : The structure of $Mg(BH_4)_2$ [10].The boron–magnesium distances (in blue) are all equal to 2.416 Å and the boron–boron distances are 4.022 and 3.786 Å (in red). (Right) The top view of the conventional cell projected along [00-1] direction [10]. Green: magnesium, pink: boron, white: hydrogen.....	35

- Figure 5.3** : $Mn(BH_4)_2$ structure by the substitution of the Mg with Mn in the structure of $Mg(BH_4)_2$ [10]. a) The variable-cell DFT optimized geometry with a symmetry of $C1m1$ (IT: 8). The DFT calculations with atomic coordinate and lattice relaxations were performed to two formula units ($Z=2$) of $Mn(BH_4)_2$. b) Tetrahedral coordination of BH_4 groups around the Mn atom in Figure (a), and its bond lengths (in Å). Representation of colors in (b); purple: manganese (Mn), pink: boron (B), white: hydrogen (H). 35
- Figure 5.4** : Ref [69] $Mn(BH_4)_2$ structure and the coordination of its atoms are illustrated. a) $Mn(BH_4)_2$ structure from Ref [69]. It has eight formula units of $Mn(BH_4)_2$ ($Z=8$) in the unit cell. b) Coordination of six BH_4 groups around the Mn atom in (a) (bond distances in Å). Representation of colors in (a); black (large): managanese (Mn) , blue: boron (B) and green: hydrogen (H). 36
- Figure 5.5** : Relaxed Ref [69] $Mn(BH_4)_2$ structure and the coordination of its atoms are illustrated. a) The variable-cell DFT optimized structure shown in Figure 5.4a. The resulting structure was found to be a monoclinic structure with a symmetry $C12/c1$ (IT: 15). b) Coordination of six BH_4 groups around the Mn atom in (a) (bond distances in Å). 37
- Figure 5.6** : The resulting $Mn(BH_4)_2$ structures obtaining from the improved CASPESA method; second iteration structures, a) only atomic coordinates were optimized, b) variable-cell optimization was carried out. 38
- Figure 5.7** : The coordinations of $Mn(BH_4)_2$ structures obtaining from the improved CASPESA method. a) Coordination of three BH_4 groups around Mn atoms of structure shown in Figure 5.6a. b) Coordination of three BH_4 groups around Mn atoms of structure shown in Figure 5.6b (bond distances in Å). 38
- Figure 5.8** : The experimental $LiMg(BH_4)_3(NH_3)_2$ structure, its relaxed structure and the coordination of atoms of the experimental structure are shown. a) The experimental $LiMg(BH_4)_3(NH_3)_2$ [16] structure. (Symmetry $P6_3$, IT:173), b) The variable-cell DFT relaxation of the experimental structure shown in (a). (Symmetry $P6_3$, IT:173) and c) Octahedral coordination of BH_4 groups around Li in the experimental structure shown in (a) (bond distances in Å). Representation of colors in (a) and (b); green (big): lithium (Li), dark green (small): boron (B), blue: nitrogen (N), white: hydrogen (H). Representation of colors in (c); purple: lithium (Li), pink: boron (B), white: hydrogen (H). 40
- Figure 5.9** : The resulting $LiMg(BH_4)_3(NH_3)_2$ structure and the coordination of its atoms. a) The $LiMg(BH_4)_3(NH_3)_2$ structure (symmetry $P6_3/m$, IT 176) was found with the improved CASPESA using *set 1* thresholds. b) Coordination of BH_4 groups with a trigonal planar geometry around the Li atom in structure shown in (a) (bond distances in Å). Representation of colors in (b); purple: lithium (Li), pink: boron (B), white: hydrogen (H). 43

Figure 5.10: The $LiMg(BH_4)_3(NH_3)_2$ structures found after the DFT variable-cell optimization was applied to nine CASPESA structures selected but eliminated by the algorithm in first iteration of <i>set 1</i> . Among them, these two have a symmetry: a) <i>Set 1-1</i> ($P6_3/m$, IT: 176) and b) <i>Set 1-2</i> ($P-62c$, IT: 190).....	44
Figure 5.11: $LiMg(BH_4)_3(NH_3)_2$ structures obtaining from <i>set 2</i> (Symmetry $P6_3/m$, IT: 176).	46
Figure 5.12: The $LiMg(BH_4)_3(NH_3)_2$ structures found after the DFT variable-cell optimization was applied to nineteen CASPESA structures selected but eliminated by the algorithm in first iteration of <i>set 2</i> . Among them, these nine have a symmetry: a) <i>Set 2-1</i> ($P6_3/m$, IT: 176), b) <i>Set 2-2</i> ($P6_3/m2/m2/c$, IT: 194), c) <i>Set 2-3</i> ($P1m1$, IT: 6), d) <i>Set 2-4</i> ($C1c1$, IT: 9), e) <i>Set 2-5</i> ($P-1$, IT: 2), f) <i>Set 2-6</i> ($Fdd2$, IT: 43), g) <i>Set 2-7</i> ($Ama2$, IT: 40), h) <i>Set 2-8</i> ($C1c1$, IT: 9) and i) <i>Set 2-9</i> ($C121$, IT: 5).	48
Figure 5.13: Close look to the experimental and the lowest energy CASPESA structures: a) The unit cell of the experimental $LiMg(BH_4)_3(NH_3)_2$ [16] structure. ($P6_3$, IT:173), b) another view of (a), c) <i>vc</i> -relaxed experimental $LiMg(BH_4)_3(NH_3)_2$ [16] structure. ($P6_3$, IT:173), d) another view of (c), e) The unit cell of <i>Set 2-1</i> structure. (Symmetry $P6_3/m$, IT: 176) and f) another view of (e).....	49

**FIRST-PRINCIPLES CRYSTAL STRUCTURE PREDICTION:
A METHOD DEVELOPMENT
AND ITS APPLICATION TO HYDROGEN STORAGE MATERIALS**

SUMMARY

Crystal Structure Prediction (CSP) can be achieved with the help of several computational approaches. In all algorithms developed so far CSP is first converted to a global optimization problem and then this is solved by mostly heuristic methods. CrystAl Structure PrEdiction via Simulated Annealing (CASPEsa) is one the recently developed approach for CSP. In this study, the capabilities of CASPEsa have been improved using the guidance of Density Functional Theory (DFT). This new method has been applied to determine the crystal structures of promising hydrogen storage materials which are suitable for on-board applications due to their high gravimetric and volumetric densities. In particular, a metal borohydride, $Mn(BH_4)_2$ and an Ammine Metal Borohydride(AMB), $LiMg(BH_4)_3(NH_3)_2$ have been selected for both of which their experimental crystal structure elucidations were already carried out. In this study, new crystal structures for both $Mn(BH_4)_2$ and $LiMg(BH_4)_3(NH_3)_2$ have been found via the newly improved CASPEsa method.

For $Mn(BH_4)_2$, the space group symmetries of the lowest two energy structures were found to be $C1m1$ and $C1c1$. In these structures, trigonal planar geometries were found unlike the experimental one having tetrahedral geometries. Besides the improved CASPEsa method, the DFT calculations with the optimizations of the internal atomic coordinates and lattice parameters of the structure by substituting Mg in $Mg(BH_4)_2$ with Mn were carried out and resulted in a structure having the symmetry of $C1m1$. In this structure, metal atoms were tetrahedrally surrounded by four BH_4 groups. The DFT calculations with the optimizations of the internal atomic coordinates and lattice parameters of another proposed $Mn(BH_4)_2$ were also carried out and resulted in a $C12/c1$ symmetry structure in which Mn coordinated with six BH_4 groups by an octahedral arrangement.

For $LiMg(BH_4)_3(NH_3)_2$, the method found the lower energy structure than the experimental one with $P6_3/m$ symmetry. In addition to the improved CASPEsa method, the extra computations of the non-chosen structures in the iteration where the lowest energy structure was found in the method were carried out and resulted in more stable structures than the experimental structure with $P6_3/m$, $P-62c$, $P6_3/m2/m2/c$, $C121$ symmetries. The less stable structures than the experimental one were also found with $P1m1$, $C1c1$, $P-1$, $Fdd2$, $Ama2$ symmetries. For all these $LiMg(BH_4)_3(NH_3)_2$ structures including DFT relaxed experimental structure, the coordination geometries of BH_4 groups around Li atoms were found to be trigonal planar unlike the experimental structure having octahedral geometries.

**AB INITIO KRİSTAL YAPI TAHMİNİ:
METOT GELİŞTİRME
VE HİDROJEN DEPOLAMA MALZEMELERİNE UYGULANMASI**

ÖZET

Kristal Yapı Tahmini (KYT) katı yapıların fiziksel özelliklerinin anlaşılması açısından çok büyük önem arz etmektedir. Özellikle deneysel olarak tam açıklanamamış veya deneyi yapılması mümkün olmayan katı bileşiklerin fiziksel özelliklerini incelemekte büyük rol oynamaktadır. Dahası KYT yeni moleküler bileşiklerin fiziksel özelliklerinin incelenmesinde de kullanılabilmesi bakımından malzeme tasarımında da büyük rol oynamaktadır. Örneğin bu çalışmada da gerçekleştirildiği gibi, bir enerji taşıyıcı olan hidrojenin depolanmasında kullanılabilecek yeni depolama malzeme önerilerinin incelenmesi KYT sayesinde gerçekleştirilebilir.

Hidrojen depolama malzemelerinde dikkat edilmesi gereken hususların başında hacimsel ve gravimetrik yoğunluklarının yüksek olması gelir. Yüksek yoğunluk daha az yer ve daha hafif olmasını sağladığı için arabalar, hafif taşıtlar gibi mobil uygulamalar açısından önem arz etmektedir. Daha sonra sıcaklık, tersinirlik, reaksiyon hızı gibi hususlar göz önüne alınır. Bu son sayılan hususlar katkı elementlerle istenen düzeylere indirgenmeye veya çıkarılmaya çalışılır. Yine bu tür yapıların incelemesi KYT ile gerçekleştirilebilir.

KYT çeşitli hesaplamalı yaklaşımların yardımı ile gerçekleştirilebilir. KYT ilk önce küresel eniyileme problemine dönüştürülür ve daha sonra bu problem keşifsel metotlar yardımıyla çözüme kavuşturulur. Benzetilmiş Tavlama yolu ile Kristal Yapı Tahmini (CASPEA) KYT için güncel olarak kurulmuş yaklaşımlardan bir tanesidir. CASPEA'nın avantajı, algoritmadaki değer fonksiyon çoğu güncel yöntemin aksine kuantum mekaniğine değil kristal yapıdan elde edilen bazı özelliklere bağlı olmasıdır. Bu da algoritmanın çok hızlı olmasını sağlarken, büyük sistemlere de uygulanmasını mümkün kılmaktadır. Bu çalışmada ise CASPEA'nın kabiliyetleri Yoğunluk Fonksiyonel Teorisi (YFT)'nin rehberliği kullanılarak geliştirilmiştir. Özel olarak geliştirilmiş analiz araçlarıyla YFT'nin CASPEA'ya bağlanmasıyla yeni bir metot önerilmiştir. Bu yeni metot, gelecek vaadeden ve yüksek hacimsel ve gravimetrik yoğunlukları nedeniyle arabalar ve hafif taşıtlar için uygun olan hidrojen depolama malzemelerine uygulanmıştır. Bu bağlamda bir metal borhidrit olan $Mn(BH_4)_2$ ve bir amin metal borhidrit (AMB) olan $LiMg(BH_4)_3(NH_3)_2$ yapıları seçilmiştir. Özellikle bu yapıların seçilmesinin nedeni ise her ikisinin de kristal yapı izahatları deneysel olarak yapılmış olması ve bu sayede yeni geliştirelen CASPEA metodunu doğrulayabilecek olmasıdır. Bu çalışmada yeni geliştirilmiş CASPEA metodu ile $Mn(BH_4)_2$ ve $LiMg(BH_4)_3(NH_3)_2$ için yeni kristal yapıları bulunmuştur.

Geliştirilmiş CASPEA metodu ilk olarak $Mn(BH_4)_2$ metal borhidrit bileşiğine uygulanmıştır. Metot uygulanmadan önce metot bulgularının karşılaştırılabilmesi için deneysel $Mn(BH_4)_2$ yapısının YFT hesaplamaları atom pozisyonlarının ve kafes parametrelerinin eniyilemeleri ile birlikte yapılmış ve YFT enerjisi bulunmuştur.

Bu eniyilemenin sonucunda deneysel yapının simetrisinin bozulmadığı saptanmıştır. Yine yöntemi uygulamadan önce, yöntem bulgularının doğruluğunu pekiştirmek için diğer teorik çalışmalardaki $Mn(BH_4)_2$ yapıları da incelenmiştir. Bunlardan birincisi teorik çalışması yapılmış $Mg(BH_4)_2$ molekülündeki Mg nin yerine Mn getirilerek oluşturulan yapıdır. Burada bu yapının YFT hesaplamaları atom pozisyonlarının ve kafes parametrelerinin eniyilemeleri ile birlikte gerçekleştirilmiş ve sonucunda $C1m1$ simetrik yapı bulunmuştur. Bu yapıda metal atomları dört yüzlü geometri oluşturacak şekilde BH_4 grupları tarafından çevrelenmiştir. Yalnız bu dört yüzlünün teorik çalışması yapılmış $Mg(BH_4)_2$ molekülüne göre biraz bozulduğu gözlenmiştir. Bu bozulma teorik çalışmada bulunan tetragonal $I-4m2$ simetrisinin monoklinik $C1m1$ simetrisine dönüşmesi neden olmuştur. Teorik çalışmaların ikincisi ise YFT çalışması yapılmış $Mn(BH_4)_2$ yapısıdır. Bu yapısında YFT hesaplamaları atom pozisyonlarının ve kafes parametrelerinin eniyilemeleri ile birlikte gerçekleştirilmiştir. Sonuç olarak Mn 'nin 6 tane BH_4 gruplarına sekiz yüzlü geometri oluşturacak şekilde bağlandığı gözlenmiş ve yapının da $C12/c1$ simetrisine sahip olduğu tespit edilmiştir. Yine bu yapıdaki sekiz yüzlü geometri, YFT çalışması yapılmış $Mn(BH_4)_2$ yapısına göre biraz bozulduğu gözlenmiştir. Yine bu bozulma teorik çalışmada bulunan ortorombik $Fddd$ simetrik yapının monoklinik $C12/c1$ simetrik yapıya dönüşmesine neden olmuştur. Deneysel yapı ve bahsedilen iki teorik çalışmadan sonra geliştirilmiş CASPESA metoduna gelindiğinde ise algoritmanın başlaması için gereken kısıtlamalar $Mn(BH_4)_2$ yapısı için hemen hemen deneysel değerlere yakın başlangıç değerleri önerilmiştir. Bunun nedeni ise ilk yöntem denemesi olduğu için algoritmanın çabuk sonuca ulaşmasının istenmesidir. Algoritma sonlandığında $Mn(BH_4)_2$ için en düşük enerjili iki yapının uzay grup simetrikleri, monoklinik kafesleri olan $C1m1$ ve $C1c1$ olarak bulunmuştur. Deneysel $Mn(BH_4)_2$ yapısındaki dörtyüzlü geometrilerin aksine bu yapılarda üçgen düzlemsel geometriler bulunmuştur. Bu üçgen düzlemseller bir yönde zincir oluşturacak şekilde kafes içinde dizilmişlerdir.

İkinci olarak, geliştirilmiş CASPESA metodu $LiMg(BH_4)_3(NH_3)_2$ AMB bileşiğine uygulanmıştır. Yine bu yöntem uygulamadan önce bulguların karşılaştırılabilmesi için deneysel $LiMg(BH_4)_3(NH_3)_2$ yapısının YFT hesaplamaları atom pozisyonlarının ve kafes parametrelerinin eniyilemeleri ile birlikte yapılmış ve YFT enerjisi bulunmuştur. Bu YFT eniyilemesinden sonra deneysel yapıda değişiklik olsada simetrisinin aynı kaldığı gözlemlenmiştir. Deneysel yapıda Li etrafında 6 tane BH_4 grupları bulunurken, eniyilemeden sonra BH_4 grupları Li etrafında üçgen düzlemsel yapı oluşturacak şekilde konumlanmışlardır. Bu deneysel yapı incelemesinden sonra yöntem uygulamasına geçildiğinde ise algoritmayı başlatmak için $LiMg(BH_4)_3(NH_3)_2$ yapısı için iki çeşit başlangıç kısıtlamaları önerilmiştir. İlk başlangıç kısıt değerleri, deneysel olarak bilinen bağ uzunluklarından 1 ila 2 Å fazla veya eksik alınarak elde edilmiştir. İkinci başlangıç kısıt değerleri ise kovalent yarıçapları dikkate alınarak oluşturulmuştur. İki atom arasındaki kovalent yarıçaplarının toplamının 2.5 katı alınarak elde edilmiştir. Her iki başlangıç değeri için geliştirilmiş CASPESA yöntemi deneysel yapıdan daha düşük enerjili, altıgen kafesli ve $P6_3/m$ simetrik yapılar bulmuştur. Geliştirilmiş CASPESA yöntemine ek olarak, yöntemin en son düşük enerjili yapı bulunan yinelemesindeki diğer seçilmeyen yapılardaki ilave hesaplamalar gerçekleştirilmiş ve sonucunda deneysel yapıdan daha kararlı $P6_3/m$, $P-62c$, $P6_3/m2/m2/c$, $C121$ simetrik yapılar bulunmuştur. Deneysel yapıdan daha az kararlı $P1m1$, $C1c1$, $P-1$, $Fdd2$, $Ama2$ simetrik yapılar da bulunmuştur. Tüm bu yapılar için, DFT eniyilemesi yapılmış deneysel yapı da dahil olmak üzere, deneysel yapının sahip olduğu sekiz

yüzlü geometrilerin aksine *Li* atomları etrafındaki BH_4 gruplarının koordinasyon geometrisinin üçgen düzlemsel olduğu bulunmuştur.

1. INTRODUCTION

Trying to establish a priori exactly how molecules come together in crystals is in fact a very difficult problem, and is known by the name Crystal Structure Prediction (CSP) [1]. CSP is a problem of formidable proportions because the solution requires a complete understanding of the mechanism for crystallization [1]. There are many computational methods [2–5] developed for CSP using simulated annealing, density functional theory, evolutionary algorithms, random sampling, basin hopping, data mining and molecular mechanics [6]. Their ultimate target are always to predict crystal structures of molecules without experimental data. A prediction using experimental data, in fact, is not real crystal structure prediction. Experimental data just confirm whether a method developed is true or not. To be genuinely predictive, a method must start from no empirically based information on the positions of the atoms in the unit cell [6]. On the other hand, there is an application part of CSP to any materials. In this context, applications of a prediction method to find some important materials can be vital. For instance, energy materials are always an indispensable research area and it is known that fossil fuels are limited. Thus new energy resources and materials are needed. In this regard, hydrogen storage materials are significant in terms of renewable energy. It is known that hydrogen is an energy carrier, which creates energy combining with oxygen (O_2) in fuel cells. Therefore, designing and finding a new storage mediums for hydrogen is very promising. Moreover, higher gravimetric and volumetric densities of hydrogen in mediums are the final targets of the storage researches since such materials can be applied to on-board applications such as automobiles, light-duty vehicles, etc. Respecting these properties, metal amines and metal borohydrides are so interesting materials for hydrogen storage. But there are several critical problems related with them. As to the metal amines, they need ammonia catalyzers to distract hydrogen. As to metal borohydrides, they need high temperatures release hydrogen.

In this study, It is aimed to improve Crystal Structure Prediction via Simulated Annealing (CASPEA) [7–14] method by adding DFT calculations together with some auxiliary analysis scripts for predicting stable and metastable crystal structures

of materials. Here a metal borohydride, $Mn(BH_4)_2$ and an Ammine Metal Borohydride (AMB), $LiMg(BH_4)_3(NH_3)_2$ were chosen. These metal borohydrides were used, because they have high gravimetric and volumetric densities, and they have experimental data [15, 16] that can verify the improved method whether it is working properly or not.

2. HYDROGEN STORAGE

Hydrogen is an element whose atomic number is 1 and symbol is H. It is the most abundant and the lightest element in the nature. Three fourth of the composition of the universe is H. At room temperature and under the normal atmosphere pressure, hydrogen is an odourless, colourless, inflammable, non-metallic, diatomic(H_2) gas. [17]. It is known as an energy carrier, which creates energy combining with oxygen (O_2) in fuel cells. It has a big prominence in energy researches, in particular due to the latter property.

2.1 Importance of Hydrogen Storage

To reduce the dependence on non-renewable energy resources, i.e. fossil fuels, energy systems based on hydrogen are necessary. Moreover, they are necessary to reduce the emission of CO_2 . Every year, the need for fossil fuels in proportion to production is increasing. Moreover, BP statistics [18] indicates that our fossil fuels are near to run out of in near future as shown in Figure 2.2. Another point is that the quarter of the world is using the energy only for transportation. For this reason, storing hydrogen inside a solid material with a high volumetric and gravimetric densities is a very vital point for the mobile applications. Another important thing is that the waste of hydrogen based energy systems is only water [19] as illustrated in Figure 2.1. In this figure, it is shown that hydrogen can be obtained by electrolysis by using solar panels [19]. Its waste is only O_2 which is necessary for life. Storage issue can be carried out by several important methods mentioned below. Storing hydrogen is relatively easier than dehydrogenation, i.e., releasing hydrogen. If the releasing part of the hydrogen cycle occurs properly for mobile applications, only one part of the cycle remains. This part is the combustion of hydrogen which is carried out by fuel cells. The waste of this part is only water. In fact, all steps of hydrogen cycle are challenging and therefore there is a huge research effort on these subjects.

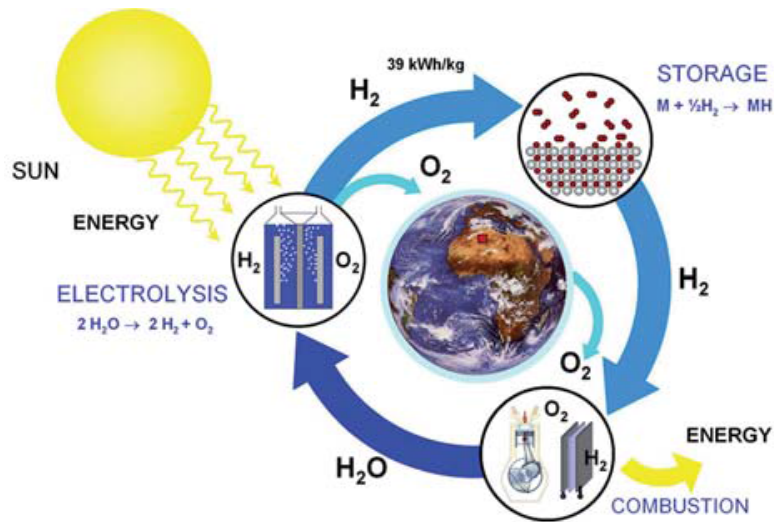


Figure 2.1: Hydrogen cycle: water dissociation by electrolysis while the oxygen is released to the atmosphere, hydrogen storage and finally combustion of hydrogen with oxygen from the atmosphere in a fuel cell or internal combustion engine. The product of the combustion is only water [18].

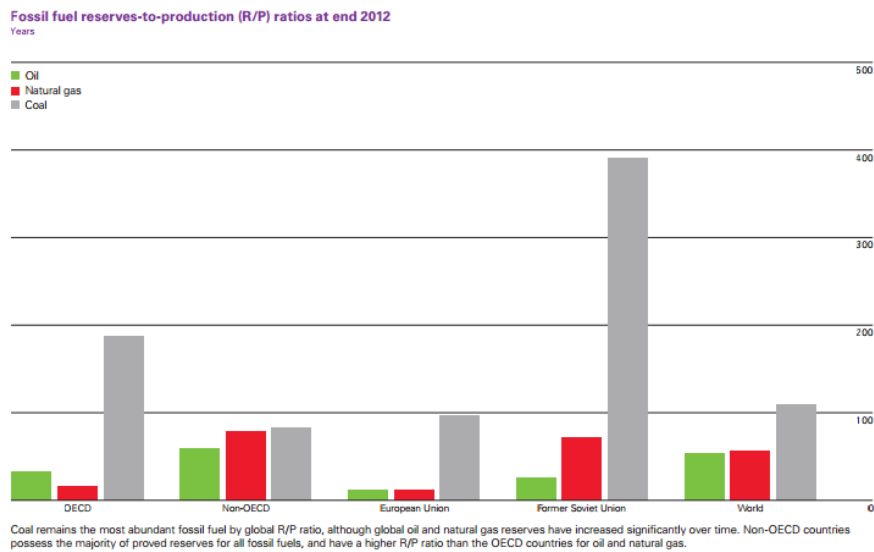


Figure 2.2: Fossil fuel reserves-to-production (R/P) ratios at end 2012 [19].

2.2 Hydrogen Storage Methods

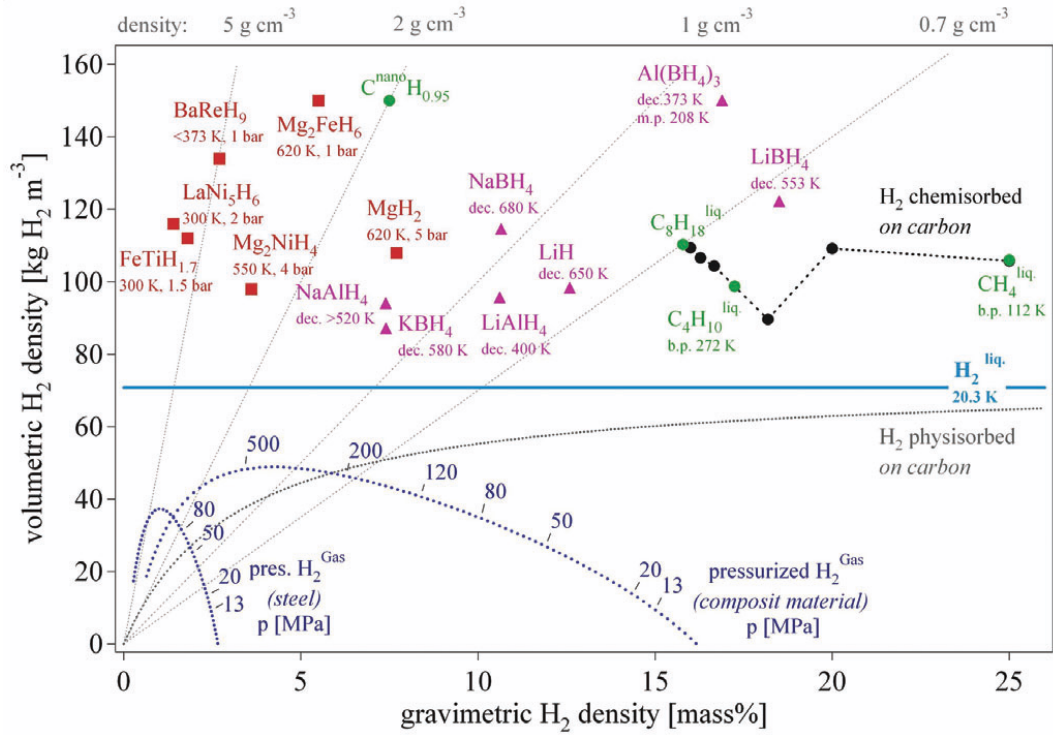
There are several hydrogen storage methods as seen on Figure 2.3. Gas and liquid hydrogen storage is possible but they require high pressures and cryogenic temperatures, i.e. near the absolute temperature [19]. Therefore, they are not

Storage method	ρ_m [mass%]	ρ_v [kg H ₂ m ⁻³]	T [°C]	p [bar]	Phenomena and remarks
High pressure gas cylinders	13	<40	RT	800	Compressed gas (molecular H ₂) in light weight composite cylinders (tensile strength of the material is 2000 MPa)
Liquid hydrogen in cryogenic tanks	size dependent	70.8	-252	1	Liquid hydrogen (molecular H ₂), continuous loss of a few % per day of hydrogen at RT
Adsorbed hydrogen	~ 2	20	-80	100	Physisorption (molecular H ₂) on materials e.g. carbon with a very large specific surface area, fully reversible
Absorbed on interstitial sites in a host metal	~ 2	150	RT	1	Hydrogen (atomic H) intercalation in host metals, metallic hydrides working at RT are fully reversible
Complex compounds	<18	150	>100	1	Complex compounds ([AlH ₄] ⁻ or [BH ₄] ⁻), desorption at elevated temperature, adsorption at high pressures
Metals and complexes together with water	<40	>150	RT	1	Chemical oxidation of metals with water and liberation of hydrogen, not directly reversible?

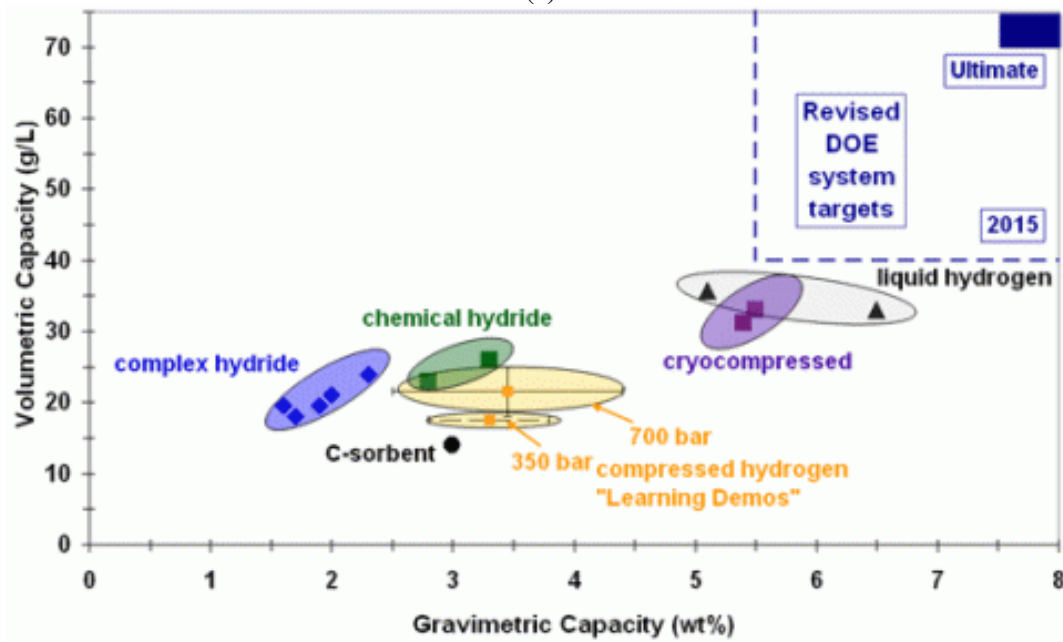
Figure 2.3: The six basic hydrogen storage methods and phenomena. The gravimetric density ρ_m , the volumetric density ρ_v , the working temperature T, and pressure p are listed. RT stands for room temperature (25°C) [20].

suitable for mobile applications. As an alternative method, metals can be used for storing hydrogen. Metals can easily adsorb H₂ molecules and they compose metal hydrides. Metal hydrides can store hydrogen with up to 3 weight(wt)% gravimetric density at room temperature (RT) and under 1 bar pressure and up to 0.150 kg/L volumetric density [20]. Disadvantages of metal hydrides are their heavy weight and low gravimetric density. Therefore, they are not suitable for on-board applications such as automobiles, light-duty vehicles, etc. Another storage method is complex hydrides. Their gravimetric and volumetric densities are higher than most of materials. But they require elevated temperatures to release hydrogen. Because of these properties they are the most interesting materials for hydrogen storage [20]. Another method uses the reaction between metal and water. For example, sodium (Na) can react with water and as a result, sodium hydroxide (NaOH) can be formed. Its gravimetric density is up to 3 wt % H. But here the major challenge of this storage method is the reversibility and control of the thermal reduction process in order to produce the metal in a solar furnace [20], however, this leads to an additional cost. Moreover, there are also methods using metal organic frames, zeolites, carbon nanotubes, etc. But, until now, they are not very successful due to low gravimetric density at ambient temperatures. Besides these direct storage methods discussed above, there is also indirect storage method, e.g., metal amines in which ammonia is stored rather than hydrogen. Although their gravimetric and volumetric densities are above the demanded level by United States Department of Energy (U.S. DOE), with 9.19 wt% and 0.115 kg/L [11], respectively, but a catalyst is required for their decomposition to hydrogen which subsequently used in pem fuel

cells. Caution must be taken in this process since existence of ammonia in pem fuel cell might poison the catalyst.



(a)



(b)

Figure 2.4: Volumetric and gravimetric hydrogen density graphs of metal hydrides and DOE targets. a) Volumetric and gravimetric hydrogen density of some hydrides. $LiBH_4$ exhibits the highest gravimetric hydrogen density of 18 mass%. [20] b) Revised United States Department of Energy (DOE) targets for hydrogen storage [21].

The DOE revised their targets because significant progress has been made on the development of hydrogen fueled vehicles. Old targets of gravimetric and volumetric densities were 9 wt% and 0.081 kg/L, respectively. New targets for 2015 are 7.5 wt% and 0.070 kg/L in Figure 2.4b [22]. In other words, for the newly developed vehicles, accommodation has been made for an additional storage system mass and volume onboard the vehicle. But the ultimate fueling rate target of the vehicles is unchanged from the previous 2015 target (2.0 kg/min) or 2.5 minutes for a 5-kg (GGE) fill of hydrogen [22].

3. CRYSTAL STRUCTURE PREDICTION

In this chapter, the principal state-of-the-art algorithms for crystal structure prediction are going to be brought up.

3.1 Crystal Structure Prediction Algorithms

There are several crystal structure prediction codes, e.g., USPEX, CALYPSO, etc. and methods. The most important of them are listed below:

3.1.1 USPEX

Universal Structure Predictor, Evolutionary Xtallography (USPEX) [23–28] is a method developed jointly by Artem R. Oganov, Andriy O. Lyakhov, Colin W. Glass and Qiang Zhu, and implemented in the same-name code written by Andriy O. Lyakhov, Colin W. Glass and Qiang Zhu. This method/code enables crystal structure prediction at arbitrary P-T conditions, given just the chemical composition of the material. This method can predict the stable and metastable structures knowing only the chemical composition. Simultaneous searches for stable compositions and structures are also possible. USPEX is interfaced with VASP, SIESTA, GULP, DMACRYS, CP2k and QuantumEspresso codes. And it also has more several properties such as the prediction of the structure of nanoparticles and surface reconstructions, powerful visualization and analysis techniques, options to optimize physical properties other than the energy, initialization using fully random approach, etc. It is efficient for systems with up to 200 atoms/cell. But its development continues to increase efficiency for larger system [2]. Until now, It has been used in many researches. Some applications of this method can be examined in the example studies [29–32].

3.1.2 CALYPSO

Crystal structure AnaLYsis by Particle Swarm Optimization (CALYPSO) [33–39] is an efficient structure prediction method. The approach requires only chemical

compositions for a given compound to predict stable or metastable structures at given external conditions (e.g., pressure and temperature), thus the CALYPSO package can be used to predict/determine the crystal structure and design the multi-functional materials (e.g., superhard). It can predict the energetically stable/metastable structures at given chemical compositions and external conditions (e.g., pressure) for clusters, 2D layers, surfaces, and 3D crystals. It can design novel functional materials. It has the options for the structural evolutions using global or local Particle Swarm Optimization (PSO). It can search the structures with automatic variation of chemical compositions. And it also can predict the structures with fixed cell parameters, or fixed space groups, or fixed molecules. CALYPSO is interfaced with VASP, CASTEP, Quantum Espresso, GULP, SIESTA and CP2K codes [3]. Some applications of this method can be examined in the example studies [40–44].

3.1.3 XtalOpt

XtalOpt [45, 46] is a free and truly open source evolutionary algorithm designed to predict crystal structures. It is implemented as an extension to the Avogadro molecular editor. XtalOpt runs on a workstation and supports using GULP, VASP, pwSCF (Quantum ESPRESSO), and CASTEP for geometry optimizations [4]. Some applications of this method can be examined in the example studies [47–49].

3.1.4 GASP

The Genetic algorithm for structure prediction (GASP) predicts the structure and composition of stable and metastable phases of crystals, molecules, atomic clusters and defects from first-principles. The GASP program is interfaced to many energy codes including: VASP, LAMMPS, MOPAC, Gulp, JDFTx and can efficiently run on parallel architectures [5]. Its developers are William W. Tipton, Ben Revard, Stewart Wenner, Richard G. Hennig. They also applied the GASP to several studies [50–54].

3.1.5 CASPESA

CrystAl Structure PrEdiction via Simulated Annealing (CASPESA) was developed by Adem Tekin and already applied to the most interesting hydrogen storage materials [7–14]. It has not been released yet. CASPESA intends to predict stable and metastable

crystal structures of materials. CASPESA has constraints, that must be defined before starting the method, such as lattice type, unit cell, bond length and objective function. These constraints can be set with the help of either experimental structure or DFT calculations.

4. COMPUTATIONAL BACKGROUND

In this chapter, the methodological explanation of Simulated Annealing (SA) and the mathematical and physical explanations of Density Functional Theory (DFT) are firstly going to be mentioned. Secondly, the improved CASPESA method which has been newly proposed in this thesis will be explained. Afterwards, the CASPESA models for the $Mn(BH_4)_2$ and $LiMg(BH_4)_3(NH_3)_2$ systems will be brought up in the section of SA setup. Finally, the DFT settings are going to be given.

4.1 Simulated Annealing

Simulated Annealing (SA) is a global optimization algorithm and a variant of it was developed by A. Corana, M. Marchesi, C. Martini, and S. Ridella [55]. There are a lot of unimodal cost function minimization algorithm (e.g. Nelder-Mead simplex method). But in the case of multimodal cost function, minimization algorithms are limited (e.g. Adaptive Random Search stochastic method). These algorithms are just efficient for the functions having several variables. However, SA is very much efficient global optimization method for the cost functions having tens of thousands of variables. SA is even successful for an ill-conditioned cost function having millions of local minima when finding the global minimum. Of course SA doesn't always guarantee to find global minimum of the cost functions but it find the nearest minimum to the global one. Another property of SA algorithm is its suitability for the continuous and non-continuous functions but both of them must, at the same time, be bounded functions [55]. Due to its peculiar features, SA in CASPESA has been used as the global optimizer.

The SA optimization algorithm can be considered analogous to the physical process by which a material changes state while minimizing its energy. A slow, careful cooling brings the material to a highly ordered, crystalline state of lowest energy. A rapid cooling instead yields defects and glass-like intrusions inside the material [55]. Here, the determination of an ideal cooling rate is a big problem. If the temperature reduction

coefficient is near to 1, the algorithm gets slower but the possibility of finding the global minimum increases. If the reduction coefficient is near to 0, the algorithm gets faster but the possibility of finding the global minimum decreases. In this study, the reduction coefficient was used to be 0.5.

4.1.1 Method

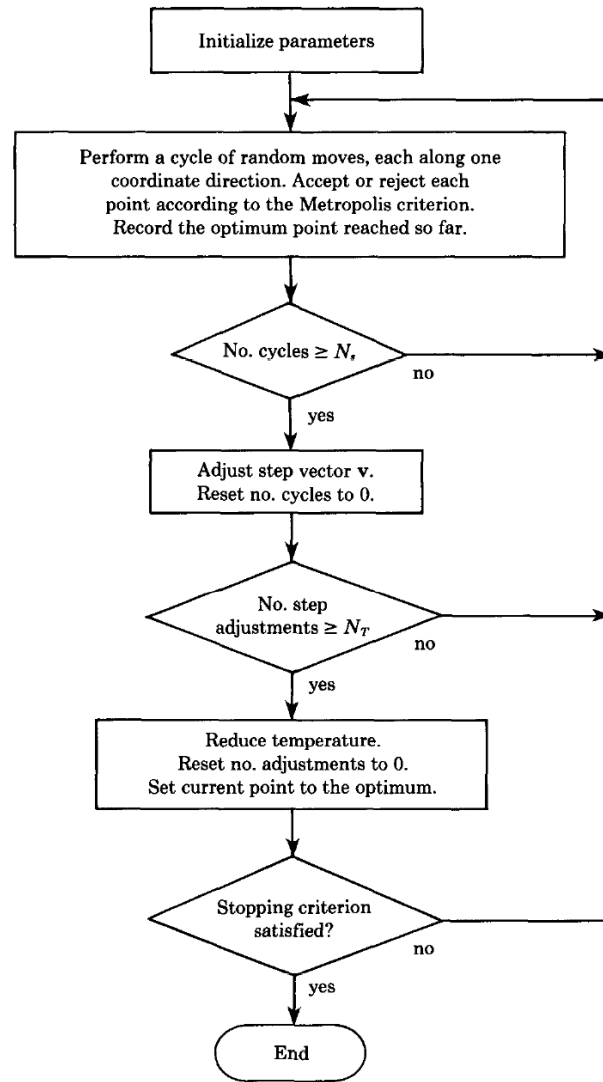


Figure 4.1: Flowchart of SA Algorithm [55].

The method of SA algorithm will be explained step by step in below. Schematic diagram of these steps is illustrated in Figure 4.1.

Let \mathbf{x} be vector in R^n : $\mathbf{x} = (x_1, x_2, x_3, \dots, x_n)$.

Let $f(\mathbf{x})$ be the function to minimize.

Let $a_1 < x_1 < b_1, \dots, a_n < x_n < b_n$ be its n variables, and each of these n variables is ranging in a finite, continuous interval.

Step 1 : Put the initial parameters,

choose \mathbf{x}_0 : starting vector.

choose \mathbf{v}_0 : starting step vector.

choose a temperature, T_0 : initial temperature.

choose a termination criterion, ϵ .

choose a number of successive temperature reductions to test for termination, N_ϵ .

choose a test for step variation, N_S .

choose a varying criterion, \mathbf{c} .

choose a test for temperature reduction, N_T .

choose a reduction coefficient, r_T .

set $i = 0, j = 0, m = 0, k = 0, h = 1$

// i :the index denoting successive points,

// j :the index denoting successive cycles along every direction,

// m :the index denoting successive step adjustments,

// k :the index denoting successive temperature reductions.

// h :the index denoting the direction along which the trial point is generated, starting from the last accepted point.

compute $f(\mathbf{x}_0)$.

set $\mathbf{x}_{opt} = \mathbf{x}_0$.

set $f_{opt} = f_0$

set $n_u = 0, u = 1, 2, 3, \dots, n$.

set $f_u^* = f_0, u = 0, -1, \dots, -N_\epsilon + 1$

Step 2 :

$\mathbf{x}' = \mathbf{x}_0 + r\mathbf{v}_{m_h}\mathbf{e}_h$

// r : a random number generated in the range $[-1, 1]$.

// \mathbf{e}_h : the vector of the h_{th} coordinate direction.

// v_{m_h} : the component of the step vector, \mathbf{v}_m , along the same direction.

Step 3 :

if $x'_h < a_h$ or $x'_h > b_h$: return to step 2.

Step 4 :

compute $f' = f(\mathbf{x}')$.

If $f' \leq f_i$:

$$\mathbf{x}_{i+1} = \mathbf{x}'$$

$$f_{i+1} = f'$$

$$i = i + 1$$

$$n_h = n_h + 1$$

if $f' < f_{opt}$:

$$\mathbf{x}_{i+1} = \mathbf{x}'$$

$$f_{opt} = f'$$

endif

else $f' > f_i$:

$$p = \exp\left(\frac{f_i - f'}{T_k}\right)$$

if $p' < p$: // p' : a pseudo random number generated in the range $[0, 1]$.

$$\mathbf{x}_{i+1} = \mathbf{x}'$$

$$f_{i+1} = f'$$

$$i = i + 1$$

$$n_h = n_h + 1$$

Step 5 :

$$h = h + 1$$

if $h \leq n$:

goto step 2.

else:

$$h = 1$$

$$j = j + 1$$

Step 6 :

if $j < N_S$:

goto step 2.

else:

update the step vector, \mathbf{v}_m

$$\text{if } n_u > 0.6N_S : \mathbf{v}'_u = \mathbf{v}_{m_u} \left(1 + c_u \frac{n_u/N_S - 0.6}{0.4} \right)$$

$$\text{else if } n_u < 0.4N_S : \mathbf{v}'_u = \left(\frac{\mathbf{v}_{m_u}}{1 + \frac{0.4 - n_u/N_S}{0.4}} \right)$$

$$\text{else: } \mathbf{v}'_u = \mathbf{v}_{m_u}$$

// u : directions

// \mathbf{v}'_u : components of the new step vector, \mathbf{v}' , in each direction u .

// c_u : the step variation along each u_{th} direction.

$$\mathbf{v}_{m+1} = \mathbf{v}'$$

$$j = 0$$

$$n_u = 0, u = 1, 2, 3, \dots, n$$

$$m = m + 1$$

Step 7 :

if $m < N_T$:

goto step 2

else:

$$T_{k+1} = r_T \cdot T_k$$

$$f_u^* = f_0$$

$$k = k + 1$$

$$m = 0$$

Step 8 : termination step,

if $|f_k^* - f_{k-u}^*| \leq \epsilon$, $u = 1, \dots, N_\epsilon$ and $f_k^* - f_{opt}^* \leq \epsilon$:

Then terminate.

else

$$i = i + 1$$

$$\mathbf{x}_i = \mathbf{x}_{opt}$$

$$f_i = f_{opt}$$

goto step 2. [55]

4.2 Density Functional Theory

4.2.1 The Schrödinger equation

The ultimate goal of most quantum mechanical approaches is the approximate solution of the time-independent, non-relativistic Schrödinger equation [56]

$$\hat{H}\Psi_i(\vec{x}_1, \vec{x}_2, \vec{x}_3, \dots, \vec{x}_N, \vec{R}_1, \vec{R}_2, \vec{R}_3, \dots, \vec{R}_M) = E_i\Psi_i(\vec{x}_1, \vec{x}_2, \vec{x}_3, \dots, \vec{x}_N, \vec{R}_1, \vec{R}_2, \vec{R}_3, \dots, \vec{R}_M) \quad (4.1)$$

where \hat{H} is the Hamilton operator for a molecular system consisting of M nuclei and N electrons in the absence of magnetic or electric fields. \hat{H} is a differential operator representing the total energy [56]:

$$\hat{H} = -\frac{1}{2}\sum_{i=1}^N \nabla_i^2 - \frac{1}{2}\sum_{A=1}^M \frac{1}{M_A} \nabla_A^2 - \sum_{i=1}^N \sum_{A=1}^M \frac{Z_A}{r_{iA}} + \sum_{i=1}^N \sum_{j>i}^N \frac{1}{r_{ij}} + \sum_{A=1}^M \sum_{B>A}^M \frac{Z_A Z_B}{R_{AB}} \quad (4.2)$$

Here, A and B run over the M nuclei while i and j denote the N electrons in the system. The first two terms describe the kinetic energy of the electrons and nuclei respectively. M_A is the mass of nucleus A in multiples of the mass of an electron. The remaining three terms define the potential part of the Hamiltonian and represent the attractive

electrostatic interaction between the nuclei and the electrons and the repulsive potential due to the electron-electron and nucleus-nucleus interactions, respectively [56].

Because of the Born-Oppenheimer approximation, we can assume nuclei are fixed and do not move, and so their kinetic energy is zero and the potential energy due to nucleus-nucleus repulsion is merely a constant. Thus the complete Hamiltonian given in (4.2) reduces to the so-called electronic Hamiltonian [56]

$$\hat{H}_{elec} = -\frac{1}{2} \sum_{i=1}^N \nabla_i^2 - \sum_{i=1}^N \sum_{A=1}^M \frac{Z_A}{r_{iA}} + \sum_{i=1}^N \sum_{j>i}^N \frac{1}{r_{ij}} = \hat{T} + \hat{V}_{Ne} + \hat{V}_{ee} \quad (4.3)$$

The solution of the Schrödinger equation with elec \hat{H} is the electronic wave function Ψ_{elec} and the electronic energy E_{elec} . The total energy E_{tot} is then the sum of E_{elec} and the constant nuclear repulsion term, E_{nuc} . [56]

$$E_{nuc} = \sum_{A=1}^M \sum_{B>A}^M \frac{Z_A Z_B}{R_{AB}} \quad (4.4)$$

$$\hat{H}_{elec} \Psi_{elec} = E_{elec} \Psi_{elec} \quad (4.5)$$

$$E_{tot} = E_{elec} + E_{nuc} \quad (4.6)$$

4.2.2 Electron density

In an electronic system, the number of the electrons per unit volume in a given state is the electron density, $\rho(\vec{r})$, for the state. This quantity is important point for the DFT. Its formula in terms of Ψ is [57]

$$\rho(\vec{r}_1) = N \int \dots \int |\Psi(\vec{x}_1, \vec{x}_2, \vec{x}_3, \dots, \vec{x}_N)|^2 ds_1 d\vec{x}_2 \dots d\vec{x}_N \quad (4.7)$$

$\rho(\vec{r})$ determines the probability of finding any of the N electrons within the volume element $d\vec{r}_1$ but with arbitrary spin while the other $N - 1$ electrons have arbitrary positions and spin in the state represented by Ψ . Strictly speaking $\rho(\vec{r})$ is a probability density, but calling it the electron density is common practice. Clearly, $\rho(\vec{r})$ is a

non-negative function of only the three spatial variables which vanishes at infinity and integrates to the total number of electrons, [56, 57]

$$\rho(\vec{r} \rightarrow \infty) = 0 \quad (4.8)$$

$$\int \rho(\vec{r}) d\vec{r} = N \quad (4.9)$$

4.2.3 Thomas-Fermi model

The first attempts to use the electron density rather than the wave function for obtaining information about atomic and molecular systems are almost as old as quantum mechanics itself and date back to the early work of Thomas and Fermi at 1927 [56]. In their model Thomas and Fermi arrive at the following, very simple expression for the kinetic energy based on the uniform electron gas, a fictitious model system of constant electron density,

$$T_{TF}[\rho(\vec{r})] = \frac{3}{10} (3\pi^2)^{2/3} \int \rho^{5/3}(\vec{r}) d\vec{r} \quad (4.10)$$

If this is combined with the classical expression for the nuclear-electron attractive potential and the electron-electron repulsive potential we have the famous Thomas-Fermi expression for the energy of an atom,

$$E_{TF}[\rho(\vec{r})] = \frac{3}{10} (3\pi^2)^{2/3} \int \rho^{5/3}(\vec{r}) d\vec{r} - Z \int \frac{\rho(\vec{r})}{r} + \frac{1}{2} \int \int \frac{\rho(\vec{r}_1)\rho(\vec{r}_2)}{r_{12}} d\vec{r}_1 d\vec{r}_2 \quad (4.11)$$

4.2.4 The Hohenberg-Kohn theorems

They proposed two theorems. The first theorem states that the external potential $V_{ext}(\vec{r})$ is (to within a constant) a unique functional of $\rho(\vec{r})$; since, in turn $V_{ext}(\vec{r})$ fixes \hat{H} we see that the full many particle ground state is a unique functional of $\rho(\vec{r})$. Namely, the ground state density uniquely specifies the external potential V_{ext} [56].

$$\rho_0 \Rightarrow \{N, Z_A, R_A\} \Rightarrow \hat{H} \Rightarrow \Psi_0 \Rightarrow E_0 \text{ and all other properties} \quad (4.12)$$

Since the complete ground state energy is a functional of the ground state electron density as shown (4.12), total energy becomes [56]

$$E_0[\rho_0] = T[\rho_0] + E_{ee}[\rho_0] + E_{Ne}[\rho_0] \quad (4.13)$$

$$E_0[\rho_0] = \int \rho_0(\vec{r})V_{Ne}d\vec{r} + T[\rho_0] + E_{ee}[\rho_0] \quad (4.14)$$

$$E_0[\rho_0] = \int \rho_0(\vec{r})V_{Ne}d\vec{r} + F_{HK}[\rho_0] \quad (4.15)$$

$F_{HK}[\rho_0]$ is the Hohenberg-Kohn functional. For an arbitrary $\rho(\vec{r})$, it becomes [56]

$$F_{HK}[\rho] = T[\rho] + E_{ee}[\rho] \quad (4.16)$$

These two parts of functionals have not explicit form. Because of this, they prevent us to solve the Schrödinger equation exactly. But $E_{ee}[\rho]$ part has an explicit classical Coulomb part $J[\rho]$ which is shown in (4.17) [56].

$$E_{ee}[\rho] = \frac{1}{2} \int \int \frac{\rho(\vec{r}_1)\rho(\vec{r}_2)}{r_{12}} d\vec{r}_1 d\vec{r}_2 + E_{ncl}[\rho] = J[\rho] + E_{ncl}[\rho] \quad (4.17)$$

$E_{ncl}[\rho]$ is the non-classical contribution to the electron-electron interaction containing all the effects of self-interaction correction, exchange and Coulomb correlation. Again it has not an explicit expression [56].

The second theorem states that $F_{HK}[\rho]$ the functional that delivers the ground state energy of the system, delivers the lowest energy if and only if the input density is the true ground state density, ρ_0 . Let $\tilde{\rho}(\vec{r})$ be a trial density which satisfies the necessary boundary conditions such as $\tilde{\rho}(\vec{r}) \geq 0$, $\int \tilde{\rho}(\vec{r})d\vec{r} = N$, and which is associated with some external potential \tilde{V}_{ext} . Then we get the (4.18). Namely, E_0 results if and only if the exact ground state density is inserted into (4.15) [56].

$$E_0 \leq E[\tilde{\rho}] = T[\tilde{\rho}] + E_{ee}[\tilde{\rho}] + E_{Ne}[\tilde{\rho}] \quad (4.18)$$

4.2.5 The Kohn-Sham approach

Kohn and Sham introduced the concept of a non-interacting reference system built from a set of orbitals (i.e., one electron functions) such that the major part of the kinetic energy can be computed to good accuracy. By this method, as much information as possible is computed exactly, leaving only a small part of the total energy to be determined by an approximate functional [56].

We know the (4.19) from HK theorem. In this equation, only $J[\rho]$ is known, while the explicit forms of the other two contributions remain a mystery [56].

$$F[\rho] = T[\rho] + J[\rho] + E_{ncl}[\rho] \quad (4.19)$$

Kohn and Sham proposed a non-interacting reference system (which means that electrons behave as uncharged fermions and therefore do not interact with each other via Coulomb repulsion) using Hartree-Fock theorem and a Slater determinant which contains Kohn-Sham orbitals, φ_i . From these orbitals, our ground state density can be written like (4.20) and it is equal to our real system of interacting electrons via chosen proper effective potential V_S [56].

$$\rho_s(\vec{r}) = \sum_i^N \sum_s |\varphi_i(\vec{r}, s)|^2 = \rho_0(\vec{r}) \quad (4.20)$$

Kohn and Sham also proposed the exact kinetic energy (4.21) of the non-interacting reference system with the same density as the real by using Hatree-Fock kinetic energy [56]. Of course, the non-interacting kinetic energy is not equal to the true kinetic energy of the interacting system, even if the systems share the same density, i. e., $T_s \neq T$. Kohn and Sham accounted for that by introducing the following separation of the functional $F[\rho]$,

$$T_s = -\frac{1}{2} \sum_i^N \langle \varphi_i | \nabla^2 | \varphi_i \rangle \quad (4.21)$$

$$F[\rho(\vec{r})] = T_s[\rho(\vec{r})] + J[\rho(\vec{r})] + E_{xc}[\rho(\vec{r})] \quad (4.22)$$

the so-called exchange-correlation energy is defined through (4.22) as

$$E_{XC}[\rho(\vec{r})] = (T[\rho] - T_S[\rho]) + (E_{ee}[\rho] - J[\rho]) = T_C[\rho] + E_{nci}[\rho] \quad (4.23)$$

The residual part of the true kinetic energy, T_C , which is not covered by T_S , is simply added to the non-classical electrostatic contributions [56].

Finally, the energy of our interacting, real system can be written as in the light of above explanations,

$$\begin{aligned} E[\rho(\vec{r})] &= T_S[\rho(\vec{r})] + J[\rho(\vec{r})] + E_{XC}[\rho(\vec{r})] + E_{Ne}[\rho(\vec{r})] \\ &= T_S[\rho(\vec{r})] + \frac{1}{2} \int \int \frac{\rho(\vec{r}_1)\rho(\vec{r}_2)}{r_{12}} d\vec{r}_1 d\vec{r}_2 + E_{XC}[\rho(\vec{r})] + \int \rho(\vec{r}) V_{Ne} d\vec{r} \\ &= -\frac{1}{2} \sum_i^N \langle \varphi_i | \nabla^2 | \varphi_i \rangle + \frac{1}{2} \sum_i^N \sum_j^N \int \int |\varphi_i(\vec{r}_1)|^2 \frac{1}{r_{12}} |\varphi_j(\vec{r}_2)|^2 d\vec{r}_1 d\vec{r}_2 \\ &\quad + E_{XC}[\rho(\vec{r})] + \sum_i^N \int \sum_A^M \frac{Z_A}{r_{1A}} |\varphi_i(\vec{r}_1)|^2 d\vec{r}_1 \end{aligned} \quad (4.24)$$

The only term for which no explicit form can be given, i. e., the big unknown, is of course E_{XC} . Similarly to what we have done within the Hartree-Fock approximation, we now apply the variational principle and ask: what condition must the orbitals φ_i fulfill in order to minimize this energy expression under the usual constraint of $\langle \varphi_i | \varphi_j \rangle = \delta_{ij}$? The resulting equations are

$$\left(-\frac{1}{2} \nabla^2 + \int \frac{\rho(\vec{r}_2)}{r_{12}} d\vec{r}_2 + V_{XC}(\vec{r}_1) - \sum_A^M \frac{Z_A}{r_{1A}} \right) \varphi_i = \left(-\frac{1}{2} \nabla^2 + V_{eff}(\vec{r}_1) \right) \varphi_i = \varepsilon_i \varphi_i \quad (4.25)$$

$$V_S(\vec{r}) = V_{eff}(\vec{r}) = \int \frac{\rho(\vec{r}_2)}{r_{12}} d\vec{r}_2 + V_{XC}(\vec{r}_1) - \sum_A^M \frac{Z_A}{r_{1A}} \quad \text{where } V_{XC} = \frac{\delta E_{XC}}{\delta \rho} \quad (4.26)$$

The approximate exchange-correlation functionals are tried to explained by Local Density Approximation (LDA) by using the idea of a hypothetical uniform electron gas. This is a system in which electrons move on a positive background charge distribution such that the total ensemble is electrically neutral [56]. In LDA, the exchange-correlation energy is

$$E_{XC}^{LDA}[\rho] = \int \int \rho(\vec{r}) \varepsilon_{XC}(\rho(\vec{r})) d\vec{r} \quad (4.27)$$

where $\varepsilon_{XC}(\rho(\vec{r}))$ is the exchange-correlation energy per particle of a uniform electron gas of density $\rho(\vec{r})$ [56].

$$\varepsilon_{XC}(\rho(\vec{r})) = \varepsilon_X(\rho(\vec{r})) + \varepsilon_C(\rho(\vec{r})) \quad (4.28)$$

ε_X , the exchange part, was derived by Bloch and Dirac. But correlation part ε_C has not explicit expression [56].

$$\varepsilon_X = -\frac{3}{4} \sqrt[3]{\left(\frac{3\rho(\vec{r})}{\pi}\right)} \quad (4.29)$$

The approximate exchange-correlation functionals can be written by using Generalized Gradient Approximation (GGA), addition to LDA, which has the gradient of the charge density, $\nabla\rho(\vec{r})$ [56].

$$E_{XC}^{GGA}[\rho] = \int \int f(\rho_\alpha, \rho_\beta, \nabla\rho_\alpha, \nabla\rho_\beta) d\vec{r} \quad (4.30)$$

4.3 The Improved CASPESA

In the original CASPESA, first an SA optimization is performed and then for the selected structures a further geometry relaxation is conducted using DFT. Moreover, all required constraints and parameters are adjusted manually. In this thesis, a new method was proposed to improve CASPESA discussed in the previous chapter. In other words, a new method adding DFT to CASPESA by analysis tools was proposed. This new method have several aims. The first is to find the most stable structure of a molecule by using a combination of simulated annealing (SA) and density functional theory (DFT) calculations. The second is to reduce and even completely remove the necessity of user control over the optimization process with the help of some analysis scripts. The third is to supply an automatic update of the all constraints considered in the optimization.

In the improved CASPESA, the iteration includes the initialization of the parameters and some control variables. The control variables are the bond constraints, cost

function, unit cell type and atomic positions in the unit cell and some other ones such as N , N_{min} , N_{iter} , N_{cyc} . N stands for the number of proper SA structures which are selected for the subsequent DFT minimizations. In this study, in general, N was set to 10. N_{min} stands for the minimum number of the structures which should be selected. In this study, N_{min} was set to 3. The flow chart of this new implementation shown in Figure 4.2 includes two parts. The main part continues until the end of the algorithm as long as the SA runs properly. The second part is executed in case if the SA part does not run properly. These two parts in the flowchart stop when they outreach the maximum iteration or maximum cycle number, which were set to 100 and 50, respectively in this study. N_{iter} and N_{cyc} actually controls the execution of these parts and their values were initially set to zero. Bond constraints and cost function are arbitrarily defined or according to the experimental data. The last requirement for the start of the algorithm is the declaration of the atomic positions and unit cell. In this study, hexagonal unit cell was used. Atomic position models are defined in the SA setup section. In this study, the unitcell was set to hexagonal since the experimental structures for AMB and metal borohydride were hexagonal. The atomic positions were randomly initiated.

The first step of the algorithm is SA which optimizes the randomly created structures using bond constraints adjusted according to experimental data or similar structures.

The second step is the analysis of the resulting structures optimized by SA to select the best ones for the subsequent DFT relaxations. In this analysis part, several criteria are evaluated such as density, similarity, value of the objective function, bond lengths, and the coordination type. Based on these criteria, at most ten distinct structures are chosen and sent to DACAPO for the DFT calculations to computing clusters by SA analysis script. Here if the number of selected structures are below N_{min} , then the algorithm tries to find better structures by applying different strategies. The first strategy is to change the selection criteria. In the default selection scheme, the coordination number around the metal atom (Mg or Li) in a region with a radius of 3.5 \AA for $Mg(BH_4)_2$, 5 \AA for $LiMg(BH_4)_3(NH_3)_2$ set 1, 3.94 \AA for $LiMg(BH_4)_3(NH_3)_2$ set 2 is set to four for $Mg(BH_4)_2$ or six for $LiMg(BH_4)_3(NH_3)_2$ and enough number of structures are structures are selected by applying bond constraint and density constraints. In case of existence of less number of chosen structures, the selection criteria is changed. For example, the coordination number around the metal atom might be taken to be five

instead of six in $LiMg(BH_4)_3(NH_3)_2$ system. Then, the selection is processed once more. If still the selection fails, then the coordination number is lowered to four from five and the selection process is repeated. If still the selection process fails, other control variables can be further changed. In case of not finding enough structures and the algorithm is not at the beginning and N_{cyc} is zero, then another SA structure is chosen to update the bond constraints and cost function. If the algorithm is just started or N_{cyc} is bigger than zero, then new bond constraints and cost function boundaries are adapted. This cycle is repeated a maximum of N_{cyc} times.

If there is no problem in the selection of enough number of SA structures, then the third step is passed into and only the atomic positions of them are further relaxed at the DFT level and N_{cyc} is set to zero.

As the fourth step, the resulting DFT structures are analyzed by DFT analysis script and the lowest energy structure is determined.

Until now, DFT optimizations concern only the atomic positions this is because of the expense of these computations. However, the better strategy is to employ a simultaneous optimization of both unit cell and atomic positions, namely, full geometry or variable-cell optimization. Therefore, as the fifth step, for the SA structure of the lowest energy DFT structure determined in fourth step, a further DFT relaxation including also the unitcell optimization are carried out.

Then, in the sixth step, the total energy obtained from DFT optimization including only atomic positions and the one including both the unitcell and the atomic positions (variable-cell) are compared. The variable-cell optimization leads to lower energies.

Then, in the seventh step, the lowest energy obtained in this iteration is compared with the one obtained at the previous iteration. Of course, it should be noted that this energy comparison is left out in first iteration. If the previous one has a lower or equal energy than the newest one or N_{iter} outreaches the max iteration number, the algorithm is terminated. Otherwise, the algorithm iterates again updating the constraints and cost function by using the parameters derived from the lowest energy structure by DFT analysis script.

The biggest contribution of the new algorithm to CASPESA is the automatic adjustment of bond constraints and cost function leading to an iterative solution.

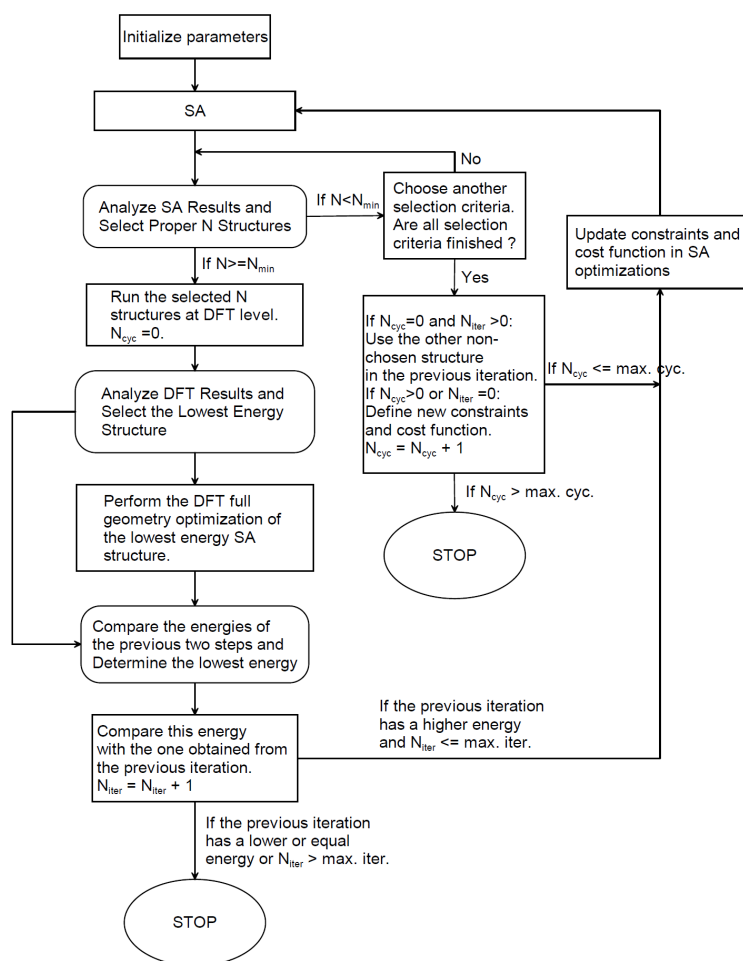


Figure 4.2: Flowchart of the improved CASPESA method.

Moreover, SA and DFT structure analysis scripts are also crucial for a successful optimization. In these scripts, bond distances are computed and these computed distances are compared with the bond distance between two atoms with the summation of their covalent bond radii [58–60]. In general, tetrahedral or octahedral coordination of metal atoms are highly energetically favourable orientations. Therefore, increasing the number of these special arrangements might lower the energy of the crystal structure. The current algorithm finding the coordination number can be run for any type of coordination. The most important difficulty of this approach is the DFT and SA parts which require parallel computations performed at high performance computing centers (the main program of SA is serial but the constructed models by SA can be sent to parallel computers). In order to have a fully automatic algorithm, all the DFT jobs must be submitted via the script and their results must also be collected by the script. However, one can easily face with some unexpected problems caused by the

high performance computing (HPC) centers preventing to operate a fully an automated script.

4.3.1 SA setup

4.3.1.1 $Mn(BH_4)_2$

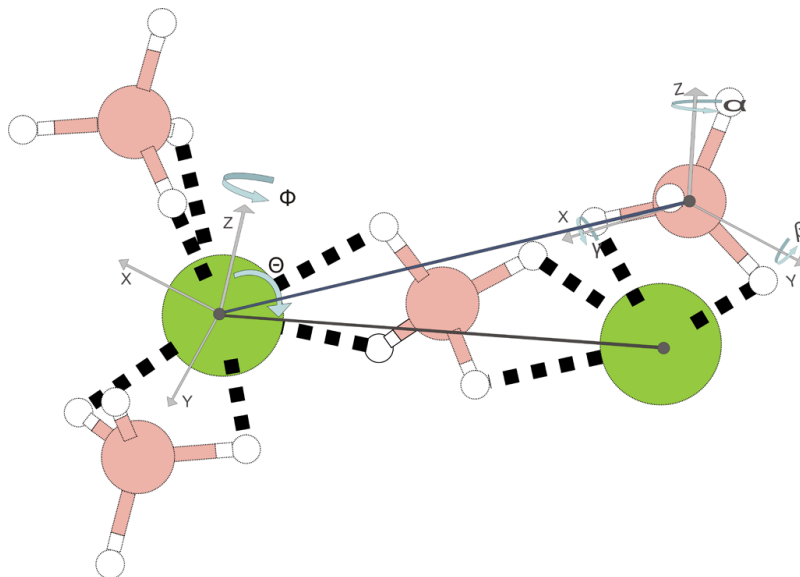


Figure 4.3: CASPEsa model of $Mn(BH_4)_2$ [10]. Representation of colors; green: manganese (Mn), pink: boron (B), white: hydrogen (H).

To run the improved CASPEsa algorithm, it is needed a unit cell, predefined bond distances and a cost function. The unit cell and atomic positions in the unit cell are completely determined using a model shown in Figure 4.3. A similar model was proposed previously for $Mg(BH_4)_2$ [10]. The model in the Ref [10] and the current one differs from $Mg(BH_4)_2$ with the employment of different bond distance criteria and cost function. As already mentioned for $Mg(BH_4)_2$ [10], maximizing the number the number of Mn–H bonds (i.e. objective function) within $(2 \times 2 \times 2)$ cut-through lattice of $Mn(BH_4)_2$ using only several bond length constraints is very important to stabilize the crystal structure. In this model, two formula units of $Mn(BH_4)_2$ were used in the unit cell. One of the Mn atom was set to the origin. A fixed tetrahedral coordinate system was used for BH_4 with B–H distances to be 1.24 Å. The positions of the other Mn atom and BH_4 groups were determined using three spherical coordinates: the centre of mass distance, Θ and Φ angles. Three euler angle parameters (α , β and γ) were used to rotate each BH_4 group. The lattice vectors were used as parameters. The resulting

36 parameters were globally optimized to maximize the number of Mn–H bonds in $Mn(BH_4)_2$. For each optimization, a crystal lattice type e.g., cubic is selected and in general all lattice types should be invoked to guarantee the search of full potential energy surface. However, here, only a hexagonal cell is used since the experimental structure contains a hexagonal cell. It is known that the SA optimizations are only based on the geometrical features of the studied system, i.e., there is no any energy value obtained neither by DFT nor molecular mechanics. Therefore, bond length constraints must be carefully defined inside the model to prevent any unphysical crystal structure. Namely, if the Mn–Mn, B–B, H–H internal (in unit cell), and H–H external (outside unit cell) bond distances in the (2 x 2 x 2) cut-through lattice is longer than 4.5, 3.5, 2.3, and 2.3 Å, respectively, then the crystal structure is accepted by SA. The fitness criteria (cost function) in SA optimizations, namely the total number of Mg–H bonds in the cut-through lattice, are determined by simply counting the number of Mn–H bonds, for the Mn–H bond in the range from 1.9 to 2.3 Å. The randomly produced structures by SA are optimized according to these criteria. After finishing of SA execution, the resulting best 10 structures, chosen by SA analysis script, are employed in the DFT calculations. After the DFT calculations, If the improved CASPESA does not terminate, then these bond distance criteria and cost function will be updated based on the geometries obtained at the DFT level.

4.3.1.2 $LiMg(BH_4)_3(NH_3)_2$

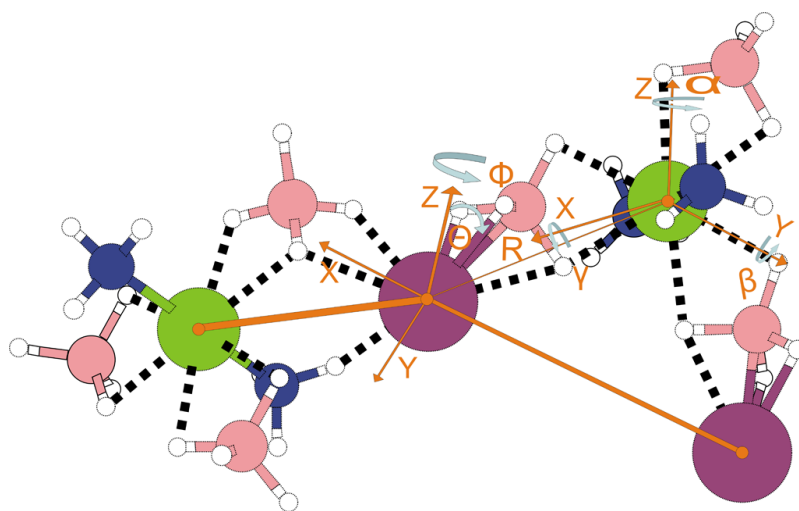


Figure 4.4: CASPESA model of $LiMg(BH_4)_3(NH_3)_2$. Representation of colors; purple: lithium (*Li*), green: magnesium (*Mg*), blue: nitrogen (*N*), pink: boron (*B*), white: hydrogen (*H*).

To create a model for $LiMg(BH_4)_3(NH_3)_2$ complex, a model of a $LiMg(BH_4)_3(NH_3)_2$ molecule for SA was constructed as shown in Figure 4.4. The same model [14] was already used with the standart CASPESA approach. In the improved CASPESA model of $LiMg(BH_4)_3(NH_3)_2$, the bond distances are first set to be far away from the experimantal data. Ultimately, it has been aimed that bond distances are evolved enough to produce crystal structures which are similar to the experimental structure. In the improved CASPESA method, the unit cell has two formula units of $LiMg(BH_4)_3(NH_3)_2$. A fixed coordinate system is used for $Mg(BH_4)_3(NH_3)_2$. As seen on Figure 4.4, NH_3 and BH_4 groups are coordinated to Mg as a trigonal bipyramid. A Li atom is placed to the origin and the spherical coordinates of the others are parameterized. Three Euler angle parameters (α , β and γ) are used to rotate the $Mg(BH_4)_3(NH_3)_2$ molecule. The lattice vectors are used as parameters. The resulting 24 parameters are globally optimized to maximize the number of interactions between hydrogens of BH_4 molecules and Li atoms. Because of the same reasons mentioned above for $Mn(BH_4)_2$, the assumption of hexagonal crystal structure was used. The following bond constraints was used for avoiding any unphysical structures: Mg–Mg, Li–Mg and Li–Li distances must be longer than 8.00, 6.00 and 5.00 Å, respectively. As an objective function, the number of Li–B distance (actually this is somehow equivalent to Li–H), which is between 4.00–2.00 Å, has been maximized. With the help of DFT calculations, all bond length constraints and cost funtion bond range is evolved.

4.3.2 DFT setup

DFT calculations are performed with DACAPO program which is a planewave DFT implementation [61]. The calculations in DACAPO are carried out with a cutoff energy of 340 eV for the plane wave and a cutoff of 500 eV for the density grid. The RPBE [61] functional is used for the exchange–correlation effects. In DACAPO, the ionic cores are described by ultrasoft pseudopotentials [62]. The electronic Brioullin zones are sampled with (2 x 2 x 2) k-points. Structural optimizations are performed until all forces are smaller than 0.05 eV Å⁻¹ using a quasi-Newton method [63] within the atomic simulation environment [64]. These settings are used for the geometry

optimization purpose and for the variable cell (both cell and atomic positions are relaxed) calculations, an additional stress on the cell is also computed.

By the way, space group symmetries of all structures in this study were determined by FINDSYM [65] program. And, the structures in this study were visualized by Jmol [66] and VESTA [67] programs.

5. RESULTS AND DISCUSSIONS

In this chapter, the results of the applications of the improved CASPESA method to the $Mn(BH_4)_2$ and $LiMg(BH_4)_3(NH_3)_2$ systems will be tried to be explained and talked about.

5.1 $Mn(BH_4)_2$

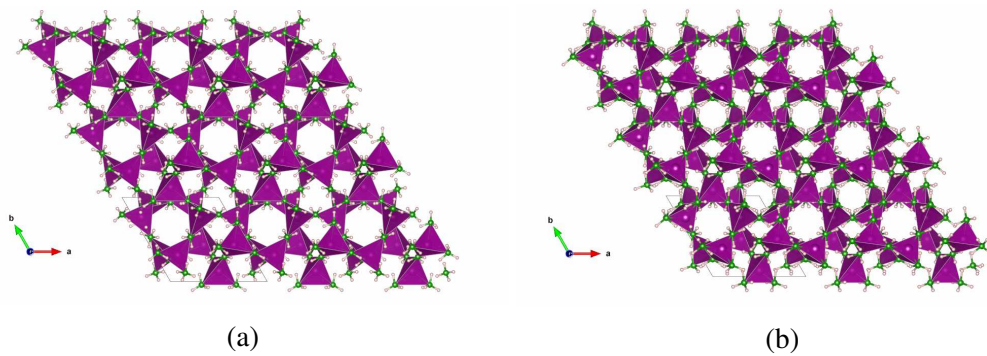


Figure 5.1: The experimental and its relaxed structures of $Mn(BH_4)_2$. a) The experimental trigonal $Mn(BH_4)_2$ [15] structure with $P3_12$ (IT: 151) symmetry. b) The variable-cell DFT optimized of the experimental $Mn(BH_4)_2$ [15]. (number of formula units of (a) and (b) in the unitcell, $Z=9$). IT represents the crystal symmetry numbers based on international tables for crystallography. Representation of colors; purple: manganese (Mn), green: boron (B), white: hydrogen (H).

Table 5.1: The minimum bond lengths of $Mn(BH_4)_2$ structures shown in Figures 5.1a and 5.1b, respectively. Here, vc (variable-cell) represents the DFT geometry optimization of the structure with the relaxations of internal atomic coordinates and lattice parameters.

Bonds (Atom-Atom)	$Mn(BH_4)_2$ [15](Å) (experimental)	$Mn(BH_4)_2$ [15](Å) (vc)
Mn-Mn	4.71	4.04
B-B	3.66	3.08
H-H_in	1.84	1.77
H-H_ex	1.84	1.77
Mn-H_up	2.31	1.86
Mn-H_low	1.89	1.65

Černý et al [15] found that $Mn(BH_4)_2$ crystallized into a trigonal lattice with a symmetry of $P3_12$ and it was stable between 90 to 450 K. Moreover, it was found

that *Mn* has a tetrahedral coordination with the BH_4 groups. *Mn-Mn* distances range from 4.71 to 4.86 Å. The cell parameters of $Mn(BH_4)_2$ were $a = 10.435$ and $c = 10.835$ Å [15]. In another experimental study for $Mn(BH_4)_2$, it was found that the ($nLiBH_4 + MnCl_2$) mixture with the molar ratios of $n = 2$ and 3 consisting mostly of $Mn(BH_4)_2$ and $LiCl$ desorbed quite rapidly about 4 wt.% H_2 at 100 °C under 1 bar H_2 pressure [68]. It was anticipated that after extraction of $LiCl$ a single-phase $Mn(BH_4)_2$ would be able to desorb about 9 wt.% H_2 at a 100-200 °C temperature range [68]. This confirms the suitability of $Mn(BH_4)_2$ for the on-board applications.

Before the application of the improved CASPESA method for $Mn(BH_4)_2$, all the available experimental and theoretical structures of $Mn(BH_4)_2$ were relaxed at the DFT level to be able to perform an energy comparison between DFT and CASPESA structures.

Firstly, the experimental structure (5.1a) were relaxed with DFT using 9 formula units ($Z=9$) in the unit cell. In this relaxations, both internal atomic coordinates and lattice parameter (vc) were carried out and the resulting geometry was shown in Figure 5.1b. The comparison of the bond lengths of the experimental structure and its resulting structure after relaxations were listed in Table 5.1. This table shows that the DFT relaxation slightly shrinks the bonds. In particular, the cost function range was changed from the range 1.89 to 2.31 Å to the range 1.65 to 1.86 Å. Nevertheless, after the relaxation, its symmetry was not altered, it remained to be $P3_112$ (IT: 151).

Second $Mn(BH_4)_2$ structure was formed by substituting the Mg atom with Mn in the $Mg(BH_4)_2$ (Figure 5.2) [10] structure which was taken from a computational study. In the Ref [10], the lowest energy structure of $Mg(BH_4)_2$ were computationally found to be tetragonal with a symmetry of $I-4m2$ (IT: 119) at 0 K. Here, variable-cell (vc) DFT calculations of this $Mn(BH_4)_2$ structure were carried out. Figure 5.3a illustrates the DFT optimized structure. No symmetry has been found for the optimized structure shown in Figure 5.3a. This might be due to the positions of hydrogen atoms. Therefore, when all hydrogens were depleted, a symmetry of $C1m1$ (IT: 8) was detected for this structure. Figure 5.3b shows that *Mn* in 5.3a has a tetrahedral bonding to BH_4 groups with a distance of 2.41 Å.

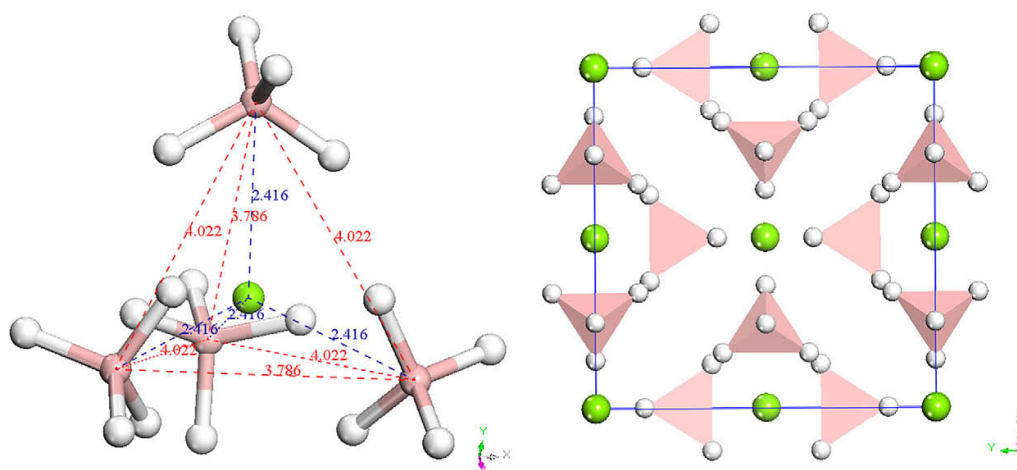


Figure 5.2: The structure of $Mg(BH_4)_2$ [10]. The boron–magnesium distances (in blue) are all equal to 2.416 Å and the boron–boron distances are 4.022 and 3.786 Å (in red). (Right) The top view of the conventional cell projected along [00-1] direction [10]. Green: magnesium, pink: boron, white: hydrogen

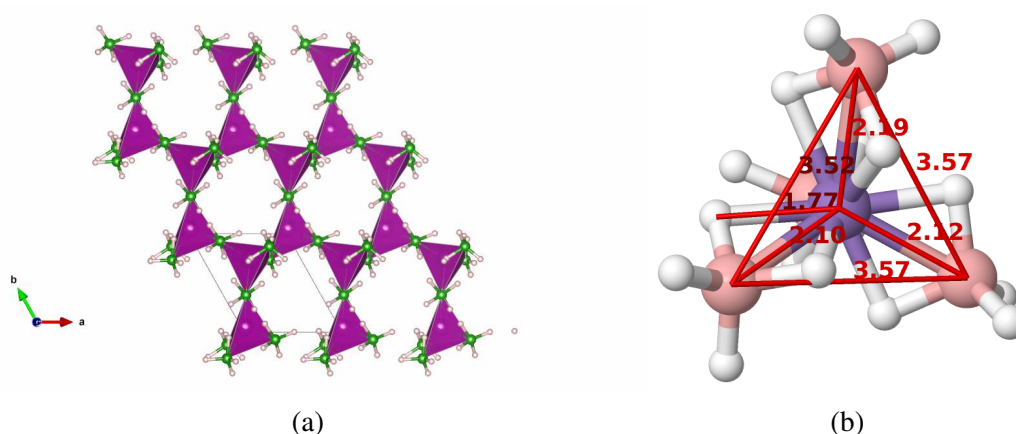


Figure 5.3: $Mn(BH_4)_2$ structure by the substitution of the Mg with Mn in the structure of $Mg(BH_4)_2$ [10]. a) The variable-cell DFT optimized geometry with a symmetry of $C1m1$ (IT: 8). The DFT calculations with atomic coordinate and lattice relaxations were performed to two formula units ($Z=2$) of $Mn(BH_4)_2$. b) Tetrahedral coordination of BH_4 groups around the Mn atom in Figure (a), and its bond lengths (in Å). Representation of colors in (b); purple: manganese (Mn), pink: boron (B), white: hydrogen (H).

As another $Mn(BH_4)_2$ structure, the crystal structure of $Mn(BH_4)_2$ shown in Figure 5.4a was found to be orthorhombic with space group $Fddd$ (IT: 70) by the DFT calculations using a unitcell containing eight formula units ($Z=8$) [69]. In the Ref [69], the shortest $Mn-H$, $B-B$ and $Mn-B$ distances were obtained to be 2.02, 3.345, 2.464 Å [69], respectively. Moreover, in this structure [69], each Mn was surrounded by six octahedrally coordinated BH_4 groups as illustrated in Figure 5.4b. The figure 5.5a

shows the variable-cell DFT relaxation of this structure. Its crystal lattice system was found to be monoclinic. All Mn were also found to be surrounded by six BH_4 groups in a distorted octahedral fashion as illustrated in Figure 5.5b. The distortion of this octahedral arrangement was severe compared to the structure shown in Figure 5.4b. This distortion clarified the reason why the structures in Figures 5.4a and 5.5a had distinct symmetries. $Mn-B$ distances were found to be 2.97-2.46 Å and 2.51-2.68 Å in the structures shown in figures 5.4b and 5.5b, respectively. The minimum bond lengths and energies of the structures shown in Figures 5.3a and 5.5a are listed in Table 5.2. As seen on Table 5.2, $Mn-H$, $B-B$ distances were shrunk in comparison with structure in Ref [69]. It seems that $Mn(BH_4)_2$ in Ref [10] is lower in energy than the one in Ref [69] by 1.27 eV as seen on Table 5.2.

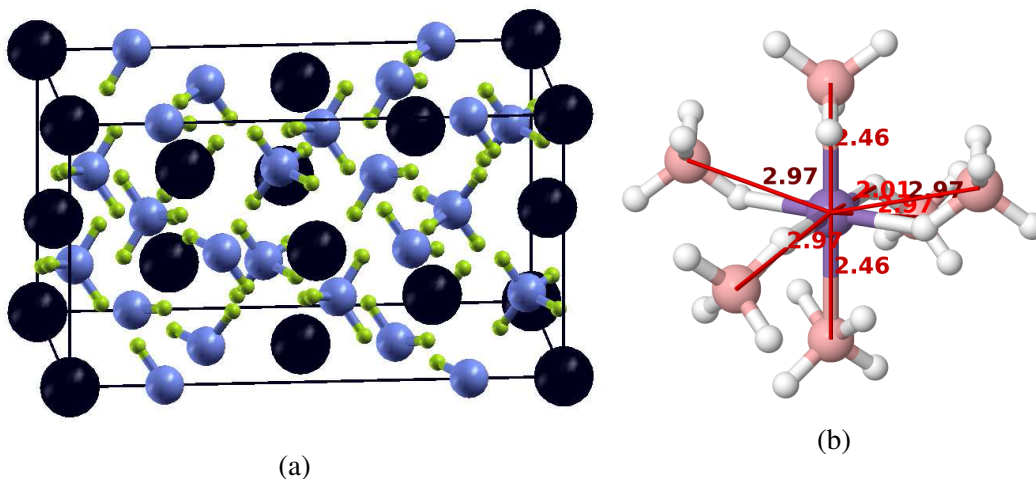


Figure 5.4: Ref [69] $Mn(BH_4)_2$ structure and the coordination of its atoms are illustrated. a) $Mn(BH_4)_2$ structure from Ref [69]. It has eight formula units of $Mn(BH_4)_2$ ($Z=8$) in the unit cell. b) Coordination of six BH_4 groups around the Mn atom in (a) (bond distances in Å). Representation of colors in (a); black (large): manganese (Mn), blue: boron (B) and green: hydrogen (H).

Following the DFT relaxations of several $Mn(BH_4)_2$ structures, the crystal structure of $Mn(BH_4)_2$ has been tried to predict by using the improved CASPESA method. All calculation setup of CASPESA and DFT was described in the previous chapter. In CASPESA, unit cell was modelled using a two f.u. of $Mn(BH_4)_2$. The algorithmic progress in the improved CASPESA method summarized in Table 5.3. In particular, it shows the change in minimum bond distances, cost function boundaries ($Mn-H_{up}$ and $Mn-H_{low}$) and the DFT energies obtained performing either atomic coordinate (ac) or variable-cell (vc) relaxations. The bond distances listed in Table 5.3

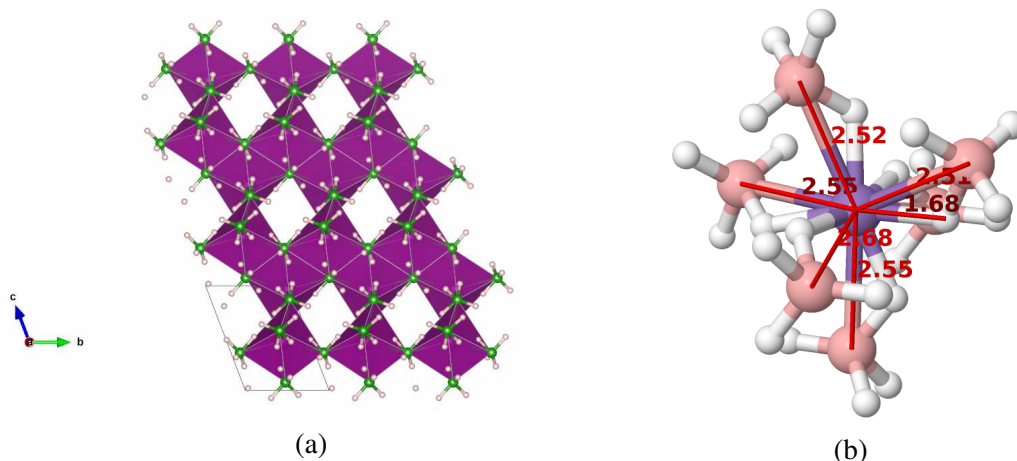


Figure 5.5: Relaxed Ref [69] $Mn(BH_4)_2$ structure and the coordination of its atoms are illustrated. a) The variable-cell DFT optimized structure shown in Figure 5.4a. The resulting structure was found to be a monoclinic structure with a symmetry $C12/c1$ (IT: 15). b) Coordination of six BH_4 groups around the Mn atom in (a) (bond distances in Å).

Table 5.2: The minimum bond lengths and energies of $Mn(BH_4)_2$ structures (for which variable-cell (*vc*) optimizations were carried out) shown in Figures 5.3a and 5.5a, respectively.

Bonds (Atom-Atom)	$Mg(BH_4)_2$ [10](Å)	$Mn(BH_4)_2$ [69]
Mn-Mn	4.05	3.77
B-B	3.20	2.91
H-H _{in}	1.88	1.73
H-H _{ex}	1.92	1.76
Mn-H _{up}	1.88	2.68
Mn-H _{low}	1.68	1.72
Energy(eV/f.u.)	-928.3623	-927.0890

are obtained from the structures which relaxed considering either only the atomic coordinates (*ac*) or also the unit cell (variable-cell). These relaxations were performed fourth and fifth steps of the improved CASPESA approach for each iteration. In all DFT minimizations (atomic coordinate and variable-cell), the initial structure has been chosen to be the one produced by SA. After the first iteration, the total energies obtained from the *ac* and *vc* optimizations were compared and the bond distance thresholds and the cost function were readjusted based on the lowest energy structure. In the first iteration, the variable-cell optimization led to the lowest energy. In table 5.3, $H-H_{in}$ is the minimum allowed hydrogen-hydrogen distance

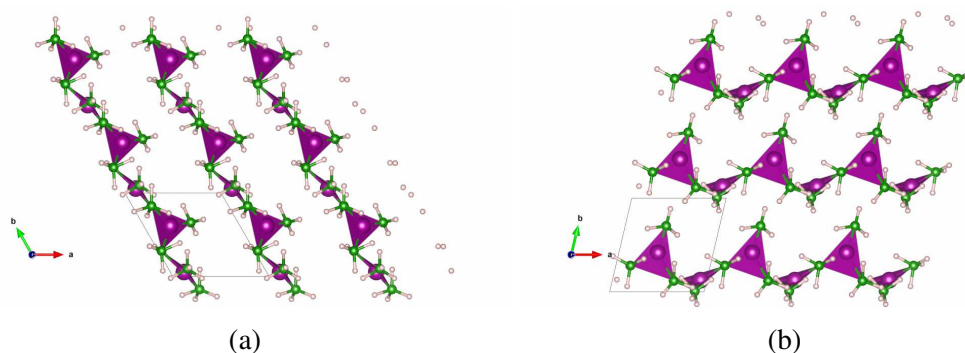


Figure 5.6: The resulting $Mn(BH_4)_2$ structures obtaining from the improved CASPESA method; second iteration structures, a) only atomic coordinates were optimized, b) variable-cell optimization was carried out.

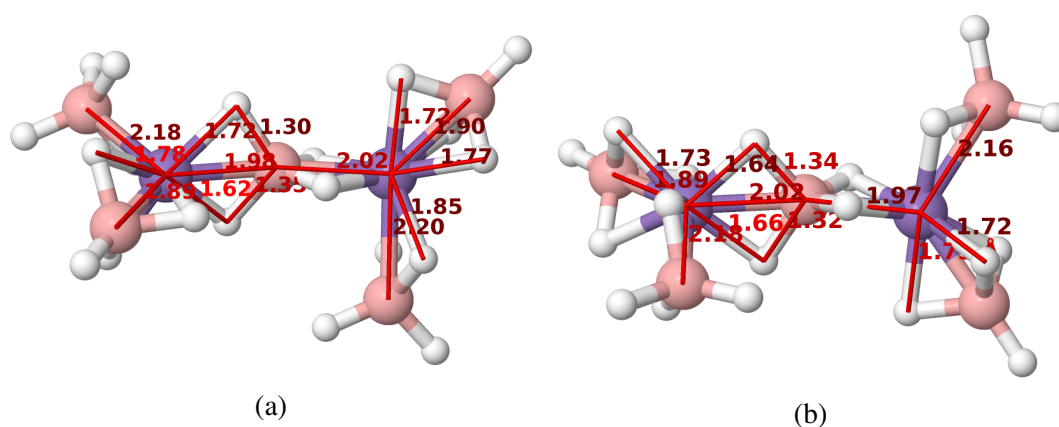


Figure 5.7: The coordinations of $Mn(BH_4)_2$ structures obtaining from the improved CASPESA method. a) Coordination of three BH_4 groups around Mn atoms of structure shown in Figure 5.6a. b) Coordination of three BH_4 groups around Mn atoms of structure shown in Figure 5.6b (bond distances in Å).

in the unitcell. $H - H_{ext}$ represents the minimum hydrogen-hydrogen distance with hydrogens existing in different units of $2 \times 2 \times 2$ repeated cell. In the second iteration, the ac -optimization gives the lowest energy structure and therefore its structural features used in the subsequent SA optimizations. In the third iteration, again the energy of the ac -optimized structure was obtained as the lowest one. However, this energy is higher than the lowest energy of the previous iteration. Thus, the algorithm was terminated at the third iteration. FINDSYM program could not assign a symmetry for the structures shown in Figures 5.6a and 5.6b. This might highly be due to the positions of the hydrogen atoms. When the hydrogens are depleted, FINDSYM starts to find monoclinic $C1m1$ (IT:8) and $C1c1$ (IT:9) symmetries for these structures, respectively. However, these monoclinic structures differ from the experimental trigonal structure.

Table 5.3: The progress of the improved CASPESA method for $Mn(BH_4)_2$. It shows how the bond constraints, cost function and energy of $Mn(BH_4)_2$ were readjusted along the iterations of the method. Bold ones indicate the lowest energy in each iteration.

Bonds (Atom-Atom)	Initial bond distances (Å)	The resulting minimum bond distances (Å)						STOP
		1.iteration		2.iteration		3.iteration		
		ac	vc	ac	vc	ac	vc	
Mn-Mn	4.50	3.83	3.78	3.84	3.81	3.87	3.90	
B-B	3.50	3.06	2.98	3.03	2.99	3.03	3.00	
H-H _{in}	2.30	1.96	1.96	1.97	1.97	1.95	1.90	
H-H _{ex}	2.30	2.04	2.06	2.02	2.01	1.97	1.90	
Mn-H _{up}	2.30	2.00	2.01	2.10	2.11	1.79	1.78	
Mn-H _{low}	1.90	1.64	1.63	1.62	1.62	1.62	1.60	
Energy (eV/f.u.)	-	-928.4301	-928.4735	-928.4913	-928.4736	-928.4486	-928.4203	

As shown in Figure 5.7, these structures have a trigonal planar BH_4 arrangements around the Mn atom in contrast to the experimental structure where Mn prefers a tetrahedral bonding of BH_4 groups. In these improved CASPESA structures shown in Figure 5.6, Mn atoms share one BH_4 group and constitute a chain along [010] and [100] directions in 5.6a and 5.6b, respectively.

Table 5.4: The cell parameters, crystal symmetries and energies of the $Mn(BH_4)_2$ structures considered in this study.

$Mn(BH_4)_2$ structure	Energy (eV/f.u.)	Space Group	a, b, c (Å)	α, β, γ (°)
CASPESA	-928.4737	$C1c1(IT : 9)$	10.673, 8.260, 6.177	90, 104, 90
Ref [10]	-928.3623	$C1m1(IT : 8)$	11.205, 7.237, 7.407	90, 128, 90
Ref [69]	-927.0890	$C12/c1(IT : 15)$	7.468, 6.607, 7.247	90, 120, 90
Experimental [15]	-927.6738	$P3_112(IT : 151)$	9.478, 9.478, 10.027	90, 90, 120

The lattice parameters, crystal symmetries and energies of the all $Mn(BH_4)_2$ structures considered in this study were listed in Table 5.4. As clear from the Table 5.4, the lowest energy structure was the one which was found via the improved CASPESA method. This was followed by the structure which was derived from $Mg(BH_4)_2$ and this structure was only 0.11 eV higher in energy. The improved CASPESA structure was also lower in energy than the experimental structure by 0.80 eV. The least stable structure was the one proposed in reference [69].

5.2 $\text{LiMg}(\text{BH}_4)_3(\text{NH}_3)_2$

It was found that $\text{LiMg}(\text{BH}_4)_3(\text{NH}_3)_2$ shown in Figure 5.8a crystallizes into an hexagonal cell (symmetry group of 173) with lattice parameters of $a = b = 8.0002 \text{ \AA}$, $c = 8.4276 \text{ \AA}$, $\alpha = \beta = 90^\circ$, and $\gamma = 120^\circ$ at 50° C [16]. Dehydrogenation studies have revealed that the $\text{LiMg}(\text{BH}_4)_3(\text{NH}_3)_2/\text{LiBH}_4$ composite is able to release over 8 wt % hydrogen below 200° C [16].

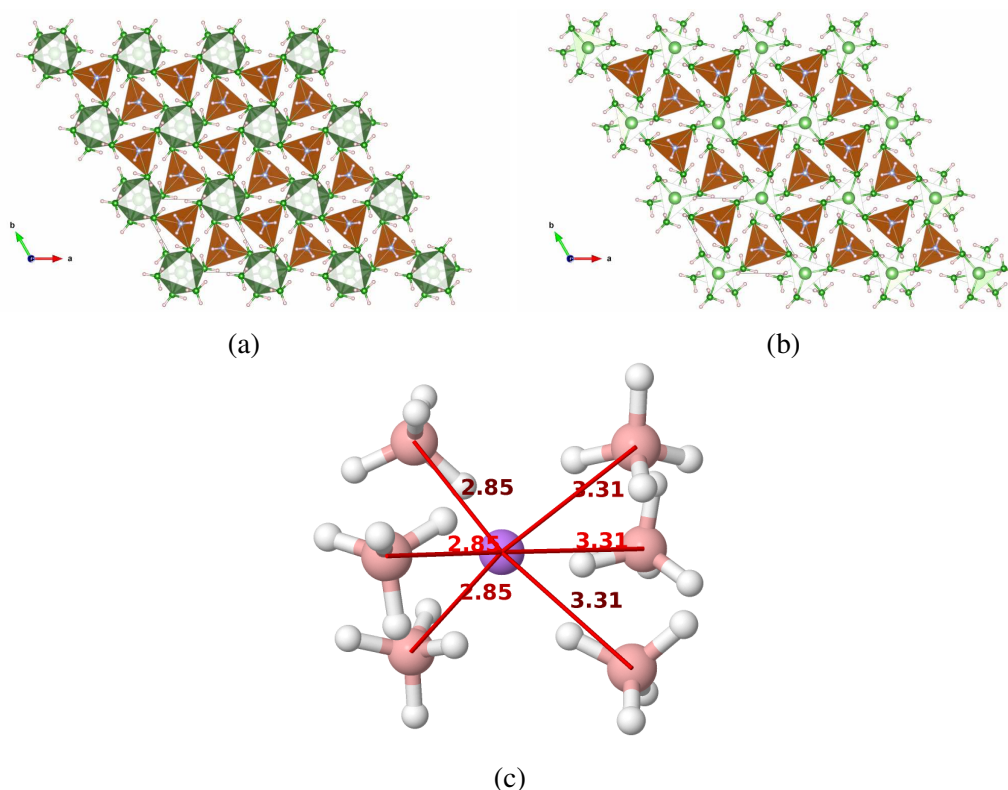


Figure 5.8: The experimental $\text{LiMg}(\text{BH}_4)_3(\text{NH}_3)_2$ structure, its relaxed structure and the coordination of atoms of the experimental structure are shown. a) The experimental $\text{LiMg}(\text{BH}_4)_3(\text{NH}_3)_2$ [16] structure. (Symmetry $P6_3$, IT:173), b) The variable-cell DFT relaxation of the experimental structure shown in (a). (Symmetry $P6_3$, IT:173) and c) Octahedral coordination of BH_4 groups around Li in the experimental structure shown in (a) (bond distances in Å). Representation of colors in (a) and (b); green (big): lithium (Li), dark green (small): boron (B), blue: nitrogen (N), white: hydrogen (H). Representation of colors in (c); purple: lithium (Li), pink: boron (B), white: hydrogen (H).

Since these properties of ammine metal borohydrides (AMB) are suitable for on-board hydrogen storage applications, the improved CASPESA method was applied to this system. First of all, the variable-cell optimization of the experimental structure was carried out and the resulting structure is shown in Figure 5.8b. A comparison between the experimental and theoretical structure can be seen in Table 5.5. This

table especially compares several bond distances used in the CASPESA algorithm, e.g, $Li - B$ distance is the cost function and $Mg - Mg$, $Mg - Li$ and $Li - Li$ are the bond thresholds. In this table, the most pronounced distance changes occurs in the cost function boundaries: from 2.85-3.31 Å (experimental) to 2.34-2.38 Å (relaxed). These remarkable changes is due to the huge structural transformation occurred after the DFT relaxation. In the experimental structure, there is an octahedral arrangement of BH_4 groups around Li atoms as shown in Figure 5.8c. However, after the relaxation, a trigonal arrangement of BH_4 groups around Li atoms appears like the one shown in Figure 5.9b. Nevertheless, the symmetry of the system is remained to be hexagonal (IT: 173).

Table 5.5: Comparison of bond thresholds and cost function boundary in the experimental (Figure 5.8a) and relaxed (Figure 5.8b) structures.

Bonds (Atom-Atom)	Experimental(Å)	Relaxed (Å)
Mg-Mg	6.18	6.54
Li-Mg	4.80	4.66
Li-Li	4.20	4.61
Li-B_up	3.31	2.38
Li-B_low	2.85	2.34

For the implementation of this AMB system into the improved CASPESA method, two different bond distance criteria were employed. First one was already described in the previous chapter and here this was called as *set 1*. The second one (*set 2*) was defined by taking 2.5 times of the summation of the covalent radii (Li: 1.24 Å, Mg: 1.27 Å, N: 0.54 Å, B: 0.73 Å, H: 0.32 Å) [58–60] of the corresponding two atoms. For $Mg-Mg$, $Li-Mg$ and $Li-Li$ distances, this formula leads to the following values 6.35, 6.27 and 6.20 Å, respectively. By using formula above, the cost function, the number of $Li-B$ bonds, is initially chosen to be in the following range: 1.97 - 4.92 Å. Note that as initial lower boundary, $Li-B_{low}$, was only the summation of their covalent radii, the initial upper boundary was obtained from the multiplication of the initial lower boundary by 2.5. In addition to these bond thresholds, another set with $Mg-Mg$: 9.00 Å, $Li-Mg$: 8.00 Å, $Li-Li$: 8.00 Å and $Li-B$: 7.00-0.00 Å was also considered. However, this set did not lead to any structure which is lower in energy than the ones obtained from *set 1*. This shows that employment of very big bond distances might lead to be trapped in some parts of the potential energy surface.

Therefore, to prevent this unwanted situation, the formula described above was used throughout the study. Another situation which might be the reason of unsatisfactory search was the value assigned for the lower boundary of Li-B. In particular, if this value sets to zero, CASPESA faces with difficulties to reach to the global minimum structure.

Table 5.6: The progress of the improved CASPESA method with using *set 1* for $LiMg(BH_4)_3(NH_3)_2$. It shows how the bond constraints, cost function and energy of $LiMg(BH_4)_3(NH_3)_2$ were readjusted along the iterations of the method. Bold ones indicate the lowest energy in each iteration.

Bonds (Atom-Atom)	Initial bond distances (Å)	The resulting minimum bond distances (Å)				STOP
		1.iteration		2.iteration		
		ac	vc	ac	vc	
Mg-Mg	8.00	6.65	6.57	6.66	6.36	
Li-Mg	6.00	4.49	4.69	3.85	4.29	
Li-Li	5.00	6.29	4.63	6.66	6.29	
Li-B_up	4.00	4.47	2.37	4.97	2.53	
Li-B_low	2.00	2.13	2.35	2.23	2.30	
Energy (eV/2f.u.)	-	-4389.1159	-4389.4146	-4387.8428	-4389.0824	

The improved CASPESA optimizations using *set 1* bond distance criteria located the structure shown in Figure 5.9a as the lowest energy. In this structure, Li atoms are coordinated to three BH_4 groups as illustrated in Figure 5.9b. The progress in the improved CASPESA method using *set 1* was illustrated in Table 5.6. Here, after the second iteration, the algorithm was stopped because the lowest energy of the last iteration was higher than the previous one. The penultimate iteration was the resulting structure, i.e. *vc* relaxed structure in first iteration in Table 5.6.

For AMB, variable-cell optimization gives completely different structures compared to the alone atomic coordinates relaxation. In *set 1*, *vc* minimization leads to a structure which is 0.29 eV lower in energy than the structure relaxed with considering only atomic coordinates. Besides the energy difference, there is also a huge structural change based upon the types of relaxation. In the former one, no symmetry has been found whereas the latter shown in Figure 5.9a, converges to $P6_3/m$ (IT: 176).

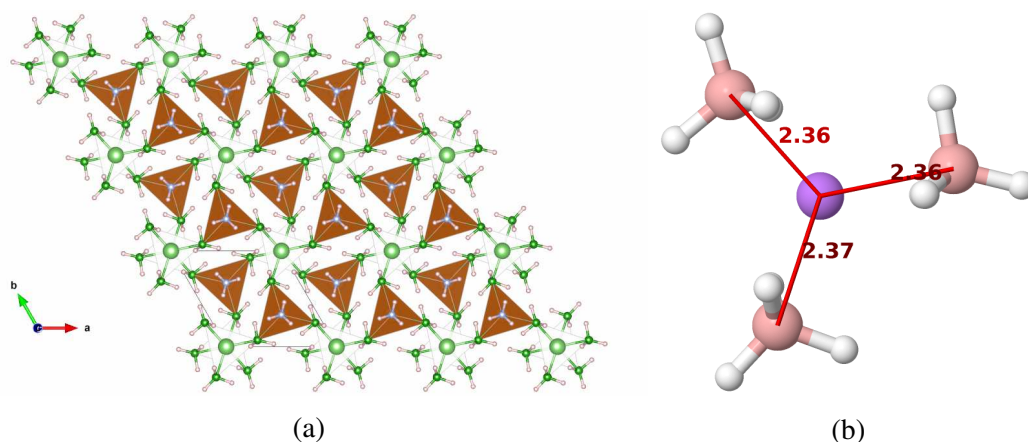


Figure 5.9: The resulting $LiMg(BH_4)_3(NH_3)_2$ structure and the coordination of its atoms. a) The $LiMg(BH_4)_3(NH_3)_2$ structure (symmetry $P6_3/m$, IT 176) was found with the improved CASPESA using *set 1* thresholds. b) Coordination of BH_4 groups with a trigonal planar geometry around the Li atom in structure shown in (a) (bond distances in Å). Representation of colors in (b); purple: lithium (Li), pink: boron (B), white: hydrogen (H).

Actually, in each iteration of the method, 10 best CASPESA structures are selected for the subsequent DFT optimizations. Among them, the lowest energy structure was found to be the one shown in Figure 5.9a. In addition to the lowest energy structure, *vc* relaxations of the remaining nine structures selected in the first iterations in *set 1* have been carried out at the DFT level. Optimizing all the selected structures at the DFT level with *vc* relaxations is our main target but due to the heavy computational time requirement, this step is not fulfilled for all system considered in this study. Among these nine structures, two symmetric low-energy structures were also found with $P6_3/m$ (IT: 176) and $P-62c$ (IT: 190) symmetries and these were shown in Figure 5.10. Table 5.7 includes the minimum bond distances of these two structures.

Table 5.7: The minimum bond and total energies of structures shown in Figure 5.10

Bonds (Atom-Atom)	Structures	
	Set 1-1 (Å)	Set 1-2 (Å)
Mg-Mg	6.60	6.66
Li-Mg	4.69	4.71
Li-Li	4.65	4.76
Li-B _{up}	2.36	2.35
Li-B _{low}	2.36	2.35
Energy(eV/2f.u.)	-4389.4238	-4389.3918

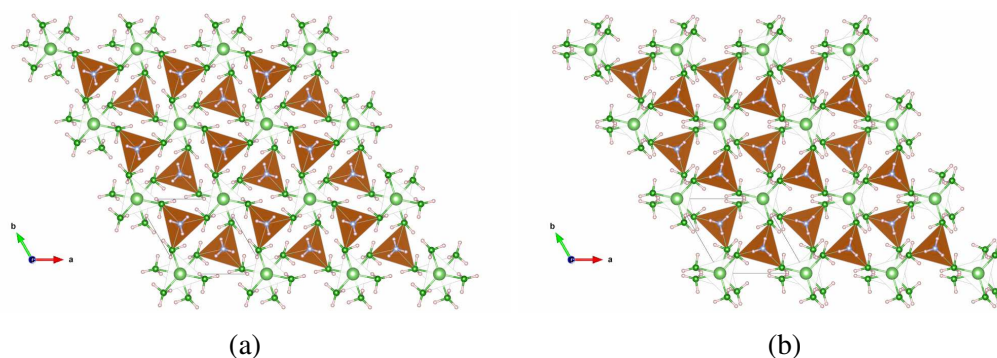


Figure 5.10: The $LiMg(BH_4)_3(NH_3)_2$ structures found after the DFT variable-cell optimization was applied to nine CASPESA structures selected but eliminated by the algorithm in first iteration of *set 1*. Among them, these two have a symmetry: a) *Set 1-1* ($P6_3/m$, IT: 176) and b) *Set 1-2* ($P-62c$, IT: 190).

CSP with the improved CASPESA has also been performed for $LiMg(BH_4)_3(NH_3)_2$ using a different constraint set called as *set 2*. In *set 2*, the following initial values were employed: $Mg-Mg$: 6.35 Å, $Li-Mg$: 6.275 Å, $Li-Li$: 6.20 Å and $Li-B$: 1.97 - 4.92 Å. When *set 2* was employed, the lowest energy structure have been found in a hexagonal cell with $P6_3/m$ (IT: 176) symmetry similar to the results obtained using *set 1*. This structure is shown in Figure 5.11. The minimum bond distances and energy of the resulting structure were listed in the second column of the first iteration of Table 5.9 in second column of first iteration. Based on the results included in this table, it is clear that the improved CASPESA algorithm has been iterated two times and in each iteration vc-relaxation led to the lowest energy.

The comparison of the resulting minimum bond distances and total energies of the DFT relaxed experimental $LiMg(BH_4)_3(NH_3)_2$ [16] and the lowest energy structures found with *set 1* and *set 2* were listed in Table 5.8. In this table, it is apparent that minimum bond distances and cost function range of the DFT relaxed experimental structure were almost the same with ones found using *set 1* and *set 2*. This similarity also implies that these three structures should have similar structural patterns. Indeed, this is the case: in these three structures three BH_4 groups are oriented in a trigonal way around the Li atom like illustrated in Figure 5.9b. However, when the symmetries are concerned, there is a very small difference: structures found from *set 1* and *set 2* have a $P6_3/m$ (IT: 176) symmetry and the experimental one have a symmetry of $P6_3$ (IT: 173). The total energies of the structures found with *set 1* and *set 2* were 0.04

eV and 0.06 eV, respectively, lower in energy than the DFT relaxed experimental one. All of these results obtained via *set 1* and *set 2* proves the robustness and performance of the improved CASPESA method.

Table 5.8: Comparison of bond length constraints in the experimental and the structures found with the improved CASPESA method using *set 1* and *set 2*. Total energies (in eV) for two formula units were obtained from the variable-cell DFT calculations.

Bonds (Atom-Atom)	Experimental(Å) (vc)	CASPESA (<i>set 1</i>) (Å) (vc)	CASPESA (<i>set 2</i>) (Å) (vc)
Mg-Mg	6.54	6.57	6.57
Li-Mg	4.66	4.70	4.75
Li-Li	4.61	4.63	4.65
Li-B_up	2.38	2.37	2.37
Li-B_low	2.34	2.35	2.35
Energy(eV/2f.u.)	-4389.3792	-4389.4146	-4389.4425

Table 5.9: The progress of the improved CASPESA method with using *set 2* for $LiMg(BH_4)_3(NH_3)_2$. It shows how the bond constraints, cost function and energy of $LiMg(BH_4)_3(NH_3)_2$ were readjusted along the iterations of the method. Bold ones indicate the lowest energy in each iteration.

Bonds (Atom-Atom)	Initial bond distances (Å)	The resulting minimum bond distances (Å)				STOP
		1.iteration		2.iteration		
		ac	vc	ac	vc	
Mg-Mg	6.35	7.56	6.57	6.74	6.56	
Li-Mg	6.28	4.59	4.75	4.16	3.73	
Li-Li	6.20	4.02	4.65	5.81	4.05	
Li-B_up	4.93	2.60	2.37	2.48	3.22	
Li-B_low	1.97	2.20	2.35	2.21	2.16	
Energy (eV/2f.u.)	-	-4388.8376	-4389.4425	-4388.9685	-4389.0124	

Similar to *set 1*, all the selected structures (in total 20) from the SA part generated by employing the *set 2* thresholds were also further vc-relaxed at the DFT level. These optimizations led to nine structures, shown in Figure 5.12, with a symmetry (triclinic (*set 2-5*), hexagonal (*set 2-1*, *set 2-2*), monoclinic (*set 2-3*, *set 2-4*, *set 2-8*, *set 2-9*) and orthorhombic (*set 2-6*, *set 2-7*). The bond distances and energies of these nine structures are listed in Tables 5.10.

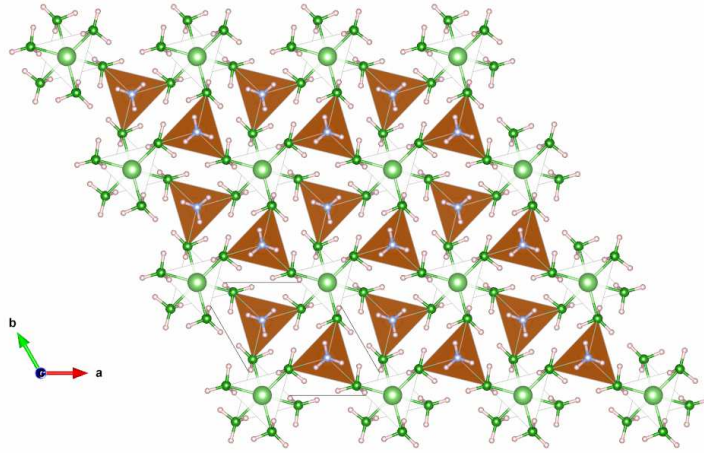


Figure 5.11: $LiMg(BH_4)_3(NH_3)_2$ structures obtaining from *set 2* (Symmetry $P6_3/m$, IT: 176).

Table 5.10: The total energies and minimum bond distances of the structures in Figure 5.12

Bonds (Atom-Atom)	Structures				
	Set 2-1 (Å)	Set 2-2 (Å)	Set 2-3 (Å)	Set 2-4 (Å)	Set 2-5 (Å)
Mg-Mg	6.60	6.64	6.40	6.28	6.36
Li-Mg	4.76	4.85	4.83	4.81	4.26
Li-Li	4.65	4.59	4.63	4.64	5.84
Li-B up	2.37	2.38	2.44	2.39	2.52
Li-B low	2.36	2.37	2.36	2.35	2.27
Energy(eV/2f.u.)	-4389.4442	-4389.4430	-4389.3400	-4389.3579	-4389.0471

Bonds (Atom-Atom)	Structures			
	Set 2-6 (Å)	Set 2-7 (Å)	Set 2-8 (Å)	Set 2-9 (Å)
Mg-Mg	6.54	6.41	6.32	6.29
Li-Mg	4.94	4.88	4.86	4.88
Li-Li	6.52	6.38	4.63	4.65
Li-B_up	2.48	2.50	2.42	2.41
Li-B_low	2.38	2.33	2.36	2.36
Energy(eV/2f.u.)	-4389.3392	-4389.3579	-4389.3743	-4389.4103

The cell parameters, energies and space groups of $LiMg(BH_4)_3(NH_3)_2$ structures obtained from *set 1* and *set 2* as well as the *vc* DFT relaxed experimental one are listed in Table 5.11. Among these structures, *set 2-1* (fig. 5.12a) was obtained to be the lowest energy one and it was only 0.07 eV lower in energy than the experimental structure. In addition, all the hexagonal structures and the monoclinic one with $C121$ symmetry found with the improved CAPESA was actually lower in energy than the experimental one [16]. On the other hand, the other structures with having different space groups (triclinic, monoclinic, orthorhombic) was found to be slightly higher in energy than the experimental structure. These findings indicate that

the improved CASPESA method is able to successfully search the potential energy surface of $LiMg(BH_4)_3(NH_3)_2$ crystal. However, CASPESA was not able to locate the experimental structure. This is because of the relaxation of this structure with DFT leads to a different structure. Since the algorithm only cares about the DFT results, even the exact experimental structure would have been found in the SA part of the algorithm, it is actually lost in the DFT treatment.

Table 5.11: Cell parameters and energies (eV) of the $LiMg(BH_4)_3(NH_3)_2$ structures found with the improved CASPESA using set 1 and set 2 in addition to the experimental structure [16].

$LiMg(BH_4)_3(NH_3)_2$ Structure	Energy (eV/2f.u.)	Space Group	a, b, c (Å)	α, β, γ (°)
Set 1	-4389.4146	$P6_3/m(IT : 176)$	8.134, 8.134, 9.269	90, 90, 120
Set 1-1	-4389.4238	$P6_3/m(IT : 176)$	8.119, 8.119, 9.328	90, 90, 120
Set 1-2	-4389.3918	$P-62c(IT : 190)$	8.166, 8.166, 9.569	90, 90, 120
Set 2	-4389.4425	$P6_3/m(IT : 176)$	8.251, 8.251, 9.312	90, 90, 120
Set 2-1	-4389.4442	$P6_3/m(IT : 176)$	8.260, 8.260, 9.293	90, 90, 120
Set 2-2	-4389.4430	$P6_3/m2/m2/c(IT : 194)$	8.419, 8.419, 9.224	90, 90, 120
Set 2-3	-4389.3400	$P1m1(IT : 6)$	8.393, 9.147, 8.424	90, 119, 90
Set 2-4	-4389.3579	$C1c1(IT : 9)$	8.315, 14.589, 9.339	90, 100, 90
Set 2-5	-4389.0471	$P-1(IT : 2)$	8.398, 8.625, 9.064	86, 81, 69
Set 2-6	-4389.3392	$Fdd2(IT : 43)$	8.648, 20.367, 14.967	90, 90, 90
Set 2-7	-4389.3579	$Ama2(IT : 40)$	10.256, 8.609, 15.048	90, 90, 90
Set 2-8	4389.3743	$C1c1(IT : 9)$	8.623, 14.620, 9.113	90, 92, 90
Set 2-9	-4389.4103	$C121(IT : 5)$	14.621, 8.530, 9.262	90, 97, 90
Experimental [16]	-4389.3792	$P6_3(IT : 173)$	8.092, 8.092, 9.212	90, 90, 120

The Figure 5.13 shows the different views of the unit cells of the experimental structure, its DFT relaxed structure and the lowest energy structure (*set 2 1*) found with the improved CASPESA algorithm. In the experimental structure shown in Figure 5.13a, *Li* is octahedrally coordinated by six BH_4 groups. However, after the DFT relaxation, there is a notable change in this structure and octahedral arrangement of BH_4 groups is cut into two trigonal coordination as shown in Figures 5.13c and 5.13d. It is also worth to mention that, in all structures found with the improved CASPESA and the experimental one, *Mg* atoms prefer a trigonal bipyramid including three BH_4 and two NH_3 groups.

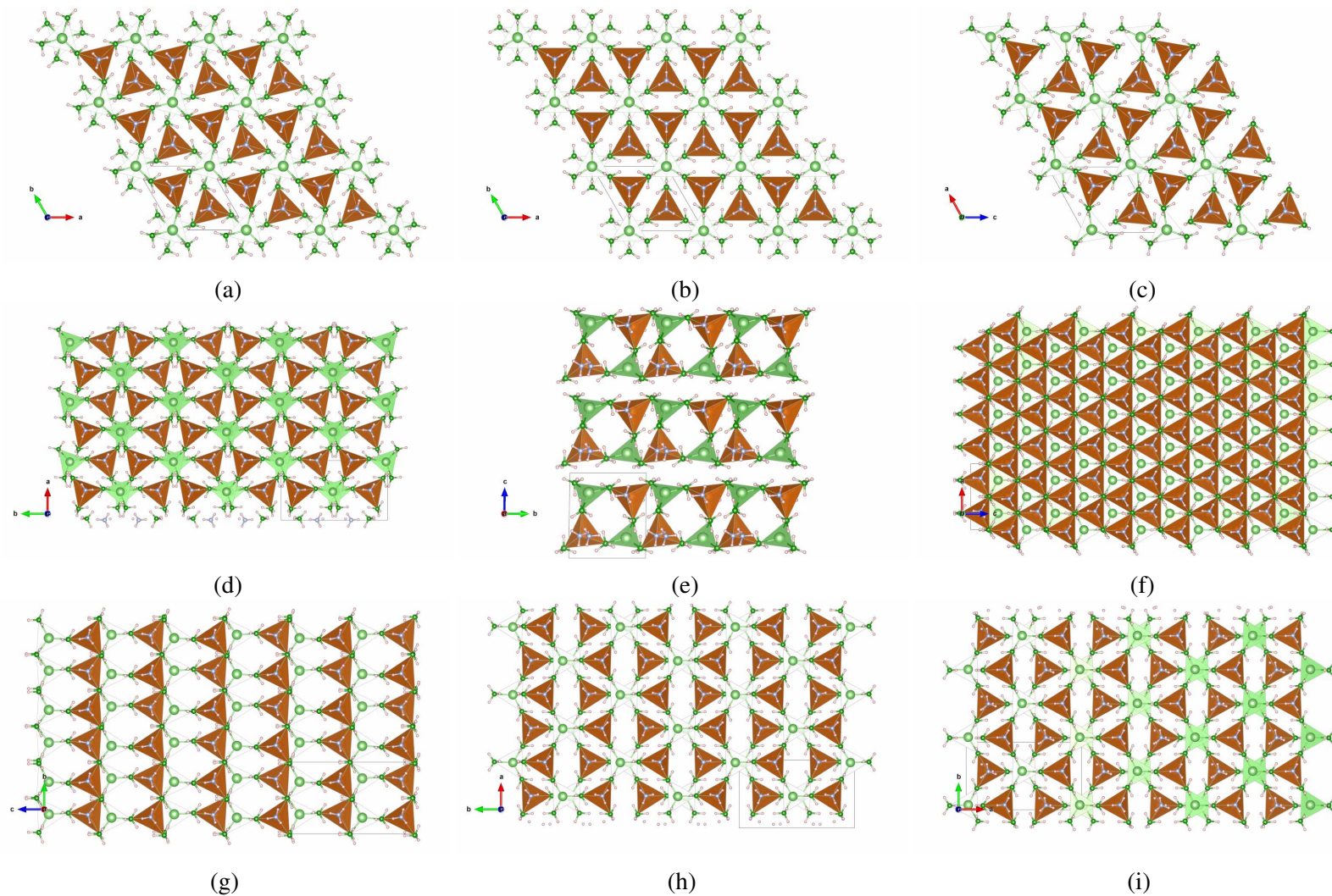


Figure 5.12: The $\text{LiMg}(\text{BH}_4)_3(\text{NH}_3)_2$ structures found after the DFT variable-cell optimization was applied to nineteen CASPESA structures selected but eliminated by the algorithm in first iteration of *set 2*. Among them, these nine have a symmetry: a) *Set 2-1* ($P6_3/m$, IT: 176), b) *Set 2-2* ($P6_3/m2/m2/c$, IT: 194), c) *Set 2-3* ($P1m1$, IT: 6), d) *Set 2-4* ($C1c1$, IT: 9), e) *Set 2-5* ($P-1$, IT: 2), f) *Set 2-6* ($Fdd2$, IT: 43), g) *Set 2-7* ($Ama2$, IT: 40), h) *Set 2-8* ($C1c1$, IT: 9) and i) *Set 2-9* ($C121$, IT: 5).

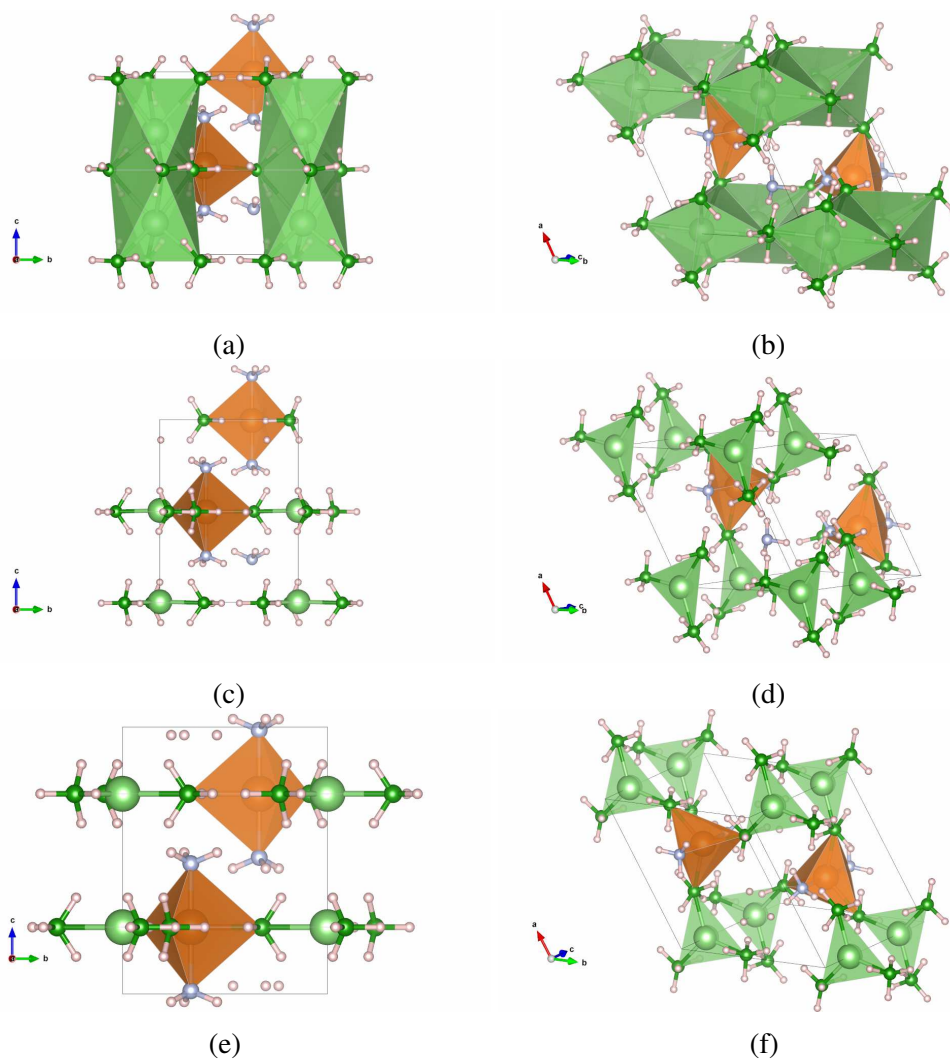


Figure 5.13: Close look to the experimental and the lowest energy CASPESA structures: a) The unit cell of the experimental $\text{LiMg}(\text{BH}_4)_3(\text{NH}_3)_2$ [16] structure. ($P6_3$, IT:173), b) another view of (a), c) *vc*-relaxed experimental $\text{LiMg}(\text{BH}_4)_3(\text{NH}_3)_2$ [16] structure. ($P6_3$, IT:173), d) another view of (c), e) The unit cell of *Set 2-1* structure. (Symmetry $P6_3/m$, IT: 176) and f) another view of (e).

6. CONCLUSIONS

In this thesis, the crystal structure prediction algorithm called as CASPESA has been improved and subsequently applied to the some peculiar hydrogen storage materials which have a potential for on-board applications. CASPESA requires some bond length constraints and a cost function which are obtained using the geometrical features of the studied system. In standard CASPESA, all these setups were adjusted with the help of either experimental structure or some preliminary DFT calculations. Then, the algorithm runs and if there is a need for resetting any constraint this can be done manually. Here, this flowchart was automated by analyzing both the DFT and CASPESA structures. In this new implementation, first, an initial constraint set and cost function are determined. Then, the CASPESA runs and the best structures from this step are selected for the subsequent DFT optimizations. After the DFT calculations, all bond length constraints and cost function are readjusted and the CASPESA reruns again. This procedure is continued until there is no any lower energy. In other words, Correcting the SA structures with DFT actually forces the SA to produce similar structures obtained with DFT. The beauty of this implementation is that after the initialization, you do not need to consider whether the constraints are correctly assigned or not. Because, they are evolved during the optimization to lead the best structures which are similar to the DFT outcomes. Another important point is that CASPESA works within a predefined lattice type, e.g., if the lattice is selected as a cubic, algorithm tries to generate crystal structures with a cubic cell. Therefore, for a full potential energy surface search all seven different lattice types must be invoked in CASPESA. Unfortunately, in this study, only the lattice types of the experimental structures were included in CASPESA. Here, this new implementation was employed to search the ground state crystal structures of $Mn(BH_4)_2$ and $LiMg(BH_4)_3(NH_3)_2$.

The improved CASPESA method was firstly applied to $Mn(BH_4)_2$ case for which there is an experimentally determined crystal structure. For this system, bond distance criteria were defined in the light of the experimental structure. Thus the improved CASPESA method was able to locate crystal structures lower in energy than the

experimental one. While *Mn* had a tetrahedral arrangement with BH_4 groups in the experimental structure, in the lowest energy structure found with the improved CASPESA approach, Mn atoms tended to form triangular coordinations with three BH_4 groups. The two other literature structures of $Mn(BH_4)_2$ were also considered. One was the structure obtained from the substitution of *Mg* with *Mn* in a $Mg(BH_4)_2$ structure, the other one was a theoretically predicted $Mn(BH_4)_2$ structure. Overall, even the improved CASPESA method was not able to reproduce the experimental structure, different structure which is lower in energy than the experimental one was found.

Two different sets of bond constraints and cost function values were used for $LiMg(BH_4)_3(NH_3)_2$. In the first attempt, bond distance criteria were assigned to be 1 or 2 Å longer than the corresponding experimental values. It has been already observed that the bond between metal and hydrogen lowers the total energy of the system. In the CASPESA model of $LiMg(BH_4)_3(NH_3)_2$, *Mg* atom forms a trigonal bipyramid with three BH_4 and two NH_3 groups. However, the coordination around the lithium was not predefined and thus it might interact with three, four or six BH_4 groups. Based on this reality, as a cost function bonding between lithium and boron atom of BH_4 groups were selected. This selection is actually similar to the employment of *Li-H* as a cost function. In particular, for the cost function the following ranges were selected for *set 1*: $2.00 \leq Li-B \leq 4.00$ and for *set 2*: $1.97 \leq Li-B \leq 4.93$. And for the stable structures, this range for both sets converged to $2.35 \leq Li-B \leq 2.37$. Moreover, another set, *set 2* for $LiMg(BH_4)_3(NH_3)_2$, was also defined by scaling the sum of the covalent bond radii of each atom forming the bond by 2.5. Since this *set 2* was as successful as *set 1*, the employment of 2.5 times of the sum of covalent radii might also be helpful for the other systems. Interestingly, the experimental structure of $LiMg(BH_4)_3(NH_3)_2$ transformed into another structure after the DFT relaxation. This structure was reproduced with the improved CASPESA method. It is quite understandable that the experimental structure has not been reproduced with CASPESA, since this structure was found to be unstable at the DFT level. In addition to the hexagonal structure which is the same with the experimental one, the improved CASPESA approach also produced new triclinic, monoclinic and orthorhombic structures which are higher in energy than the experimental one.

Currently, CASPESA is a serial code, however, it can be run in pseudo-parallel manner, if CASPESA is started on each core. CASPESA randomly assigns the optimization parameters. Thus, this will ensure the differentiation of the initial parameters and two CASPESA jobs on two cores might not converge to the same solution. In general, CASPESA had been executed 500 times and this was done by splitting the total number jobs to the number of available cores, for example, 20 CASPESA jobs were completed by each of 25 cores. This strategy certainly lowered the required computational time. In the case of DFT calculations, parallelization features of DACAPO code has been ultimately used. Employment of a cost function which is defined as the bond distance between any two atoms used only for the speed up the code. If the DFT part can be calculated within a very short time, total energy of the DFT can be ultimately used as the cost function. This situation is partially satisfied with some CSP codes for unit cells including fewer atoms.

Overall, in this study, it has been shown that the improved CASPESA approach was able to locate crystal structures of $Mn(BH_4)_2$ and $LiMg(BH_4)_3(NH_3)_2$ which are lower in energy than the experimental ones. This certainly opens a way for the employment of this new strategy to predict the crystal structures of other interesting materials.

REFERENCES

- [1] **Gautam R. Desiraju** (2002). Cryptic crystallography, *nature materials*, **1**, 77–79.
- [2] **USPEX**, <http://mysbfiles.stonybrook.edu/~aoganov/USPEX.html>, date retrieved: 22.04.2014.
- [3] **CALYPSO**, <http://www.calypso.cn/>, date retrieved: 22.04.2014.
- [4] **XtalOpt**, <http://xtalopt.openmolecules.net/wiki/index.fcgi/>, date retrieved: 22.04.2014.
- [5] **GASP**, <http://gasp.mse.cornell.edu/>, date retrieved: 22.04.2014.
- [6] **Scott M. Woodley and Richard Catlow** (2008). Crystal structure prediction from first principles, *nature materials*, **7**, 937–946.
- [7] **Riccarda Caputo and Adem Tekin** (2012). Lithium Dihydroborate: First-Principles Structure Prediction of $LiBH_2$, *Inorg. Chem.*, **51**, 9757–9765.
- [8] **Riccarda Caputo, Arkadiusz Kupczak, Wieslawa Sikora and Adem Tekin** (2013). Ab initio crystal structure prediction by combining symmetry analysis representations and total energy calculations. An insight into the structure of $Mg(BH_4)_2$, *Phys. Chem. Chem. Phys.*
- [9] **Riccarda Caputo, Adem Tekin** (2011). Ab-initio crystal structure prediction. A case study: $NaBH_4$, *Journal of Solid State Chemistry*, **184**, 1622–1630.
- [10] **Riccarda Caputo, Adem Tekin, Wieslawa Sikora, Andreas Züttel** (2009). First-principles determination of the ground-state structure of $Mg(BH_4)_2$, *Chemical Physics Letters*, **480**, 203–209.
- [11] **Adem Tekin, Jens S. Hummelshøj, Hjalte S. Jacobsen, Dadi Sveinbjörnsson, Didier Blanchard, Jens K. Nørskov and Tejs Vegge** (2010). Ammonia dynamics in magnesium ammine from DFT and neutron scattering, *Energy Environ. Sci.*, **3**, 448–456.
- [12] **Adem Tekin, Riccarda Caputo, Andreas Züttel** (2010). First-Principles Determination of the Ground-State Structure of $LiBH_4$, *Physical Review Letters*, **104**, 215501.
- [13] **Andrew J. Churchar, Ewa Banach, Andreas Borgschulte, Riccarda Caputo, Jian-Cheng Chen, David Clary, Karol J. Fijalkowski, Hans Geerlings, Radostina V. Genova, Wojciech Grochala, Tomasz Jaron, Juan Carlos Juanes-Marcos, Bengt Kasemo, Geert-Jan Kroes, Ivan Ljubic, Nicola**

- Naujoks, Jens K. Nørskov, Roar A. Olsen, Flavio Pendolino, Arndt Remhof, Lorand Romaszki, Adem Tekin, Tejs Vegge, Michael Zach and Andreas Züttel** (2011). A multifaceted approach to hydrogen storage, *Phys. Chem. Chem. Phys.*, **13**, 16955–16972.
- [14] **Yusuf Kışlak and Adem Tekin** (2014). First-Principles Structure Prediction of Dual Cation Ammine Borohydrides: $LiMg(BH_4)_3(NH_3)_x$, *International Congress on Energy Efficiency and Energy Related Materials (ENEFM2013)*, *Springer Proceedings in Physics*, (Sent, still unpublished), **60**.
- [15] **Radovan Černý, Nicolas Penin, H.H. and Filinchuk, Y.** (2009). The First Crystallographic and Spectroscopic Characterization of a 3d-Metal Borohydride: $Mn(BH_4)_2$, *J. Phys. Chem. C*, **113**, 9003–9007.
- [16] **Weiwei Sun, Xiaowei Chen, Qinfen Gu, Kia S. Wallwork, Yingbin Tan, Ziwei Tang, and Xuebin Yu** (2012). A New Ammine Dual-Cation (Li, Mg) Borohydride: Synthesis, Structure, and Dehydrogenation Enhancement, *Chemistry - A European Journal*, **18**, 9003–9007.
- [17] **Wikipedia**, <http://en.wikipedia.org/wiki/Hydrogen>, date retrieved: 22.04.2014.
- [18] **BP**, (2013), BP Statistical Review of World Energy June 2013, bp.com/statisticalreview.
- [19] **A. Züttel, A.B. and Schlapbach, L.** (2007/2008). Hydrogen As a Future Energy Carrier, *Hydrogen Report Switzerland 08/09*.
- [20] **Züttel, A.** (September 2003). Materials for hydrogen storage, *Materials Today*, 24–33.
- [21] **DOE, U.**, <http://www.energy.gov/eere/fuelcells/status-hydrogen-storage-technologies>, date retrieved: 22.04.2014.
- [22] **US DOE** (2009). Targets for Onboard Hydrogen Storage Systems for Light-Duty Vehicles, Revision 4.0, *US Department of Energy Office of Energy Efficiency and Renewable Energy and The FreedomCAR and Fuel Partnership*.
- [23] **Artem R. Oganov, Andriy O. Lyakhov, and Mario Valle** (2011). How Evolutionary Crystal Structure Prediction Works—and Why, *Accounts of Chemical Research*, **44**, 227–237.
- [24] **Artem R. Oganova, Yanming Ma, Ying Xu, Ion Errea, Aitor Bergara and Andriy O. Lyakhov** (2010). Evolutionary Crystal Structure Prediction as a Method for the Discovery of Minerals and Materials, *Reviews in Mineralogy & Geochemistry*.
- [25] **Andriy O. Lyakhova, Artem R. Oganov, Mario Valle** (2010). How to predict very large and complex crystal structures, *Computer Physics Communications*, **181**, 1623–1632.

- [26] **Artem R. Oganov and Colin W. Glass** (2008). Evolutionary crystal structure prediction as a tool in materials design, *J. Phys.: Condens. Matter*, **20**, 064210.
- [27] **Artem R. Oganov and Colin W. Glass** (2006). Crystal structure prediction using ab initio evolutionary techniques: Principles and applications, *The Journal of Chemical Physics*, **124**, 244704.
- [28] **Colin W. Glass, Artem R. Oganov, Nikolaus Hansen** (2006). US-PEX—Evolutionary crystal structure prediction, *Computer Physics Communications*, **175**, 713–720.
- [29] **Qiang Zhu, Artem R. Oganov, Miguel A. Salvado, Pilar Pertierra, and Andriy O. Lyakhov** (2011). Denser than diamond: Ab initio search for superdense carbon allotropes, *Physical Review B*, **83**, 193410.
- [30] **Guoying Gao, Artem R. Oganov, Yanming Ma, Hui Wang, Peifang Li, Yinwei Li, Toshiaki Iitaka, and Guangtian Zou** (2010). Dissociation of methane under high pressure, *The Journal of Chemical Physics*, **133**, 144508.
- [31] **Eva Zurek, Roald Hoffmann, N. W. Ashcroft, Artem R. Oganov, and Andriy O. Lyakhov** (2009). A little bit of lithium does a lot for hydrogen, *PNAS*, **106**, 17640–17643.
- [32] **V. L. Solozhenko, O. O. Kurakevych, and A. R. Oganov** (2008). On the Hardness of a New Boron Phase, Orthorhombic $\gamma - B_{28}$, *Journal of Superhard Materials*, **30**, 428–429.
- [33] **Shaohua Lu, Yanchao Wang, Hanyu Liu, Mao-sheng Miao & Yanming Ma** (2014). Self-assembled ultrathin nanotubes on diamond (100) surface, *Nature Communications*, **5**, 3666.
- [34] **Zhang, Xinxin and Wang, Yanchao and Lv, Jian and Zhu, Chunye and Li, Qian and Zhang, Miao and Li, Quan and Ma, Yanming** (2013). First-principles structural design of superhard materials, *The Journal of Chemical Physics*, **138**, 114101.
- [35] **Wang, Yanchao and Miao, Maosheng and Lv, Jian and Zhu, Li and Yin, Ketao and Liu, Hanyu and Ma, Yanming** (2012). An effective structure prediction method for layered materials based on 2D particle swarm optimization algorithm, *The Journal of Chemical Physics*, **137**, 224108.
- [36] **Lv, Jian and Wang, Yanchao and Zhu, Li and Ma, Yanming** (2012). Particle-swarm structure prediction on clusters, *The Journal of Chemical Physics*, **137**, 084104.
- [37] **Yanchao Wang, Jian Lv, Li Zhu, Yanming Ma** (2012). CALYPSO: A method for crystal structure prediction, *Computer Physics Communications*, **183**, 2063–2070.
- [38] **Xinyu Luo, Jihui Yang, Hanyu Liu, Xiaojun Wu, Yanchao Wang, Yanming Ma, Su-Huai Wei, Xingao Gong, and Hongjun Xiang** (2011). Predicting Two-Dimensional Boron–Carbon Compounds by the Global Optimization Method, *J. Am. Chem. Soc.*, **133**, 16285–16290.

- [39] **Wang, Yanchao and Lv, Jian and Zhu, Li and Ma, Yanming** (2010). Crystal structure prediction via particle-swarm optimization, *Phys. Rev. B*, **82**, 094116.
- [40] **Xu Ying, Chen Changbo, Sun Xiuping** (2014). First-principles study of high-pressure crystal structures and superconductivity of Li_3Be alloy, *Computational Materials Science*, **88**, 45–49.
- [41] **H. J. Xiang, Bing Huang, Erjun Kan, Su-Huai Wei, and X. G. Gong** (2013). Towards Direct-Gap Silicon Phases by the Inverse Band Structure Design Approach, *Physical Review Letters*, **110**, 118702.
- [42] **De Yu Wang, Bing Wang, and Yuan Xu Wang** (2012). New Crystal Structures of IrB and IrB_2 : First-Principles Calculations, *The Journal of Physical Chemistry C*, **116**, 21961–21966.
- [43] **Lv, Jian and Wang, Yanchao and Zhu, Li and Ma, Yanming** (2011). Predicted Novel High-Pressure Phases of Lithium, *Phys. Rev. Lett.*, **106**, 015503.
- [44] **Peifang Li, Guoying Gao, Yanchao Wang, and Yanming Ma** (2010). Crystal Structures and Exotic Behavior of Magnesium under Pressure, *The Journal of Physical Chemistry C*, **114**, 21745–21749.
- [45] **David C. Lonie, Eva Zurek** (2012). Identifying duplicate crystal structures: XtalComp, an open-source solution, *Computer Physics Communications*, **183**, 690–697.
- [46] **David C. Lonie, Eva Zurek** (2011). XtalOpt: An open-source evolutionary algorithm for crystal structure prediction, *Computer Physics Communications*, **182**, 372–387.
- [47] **Lonie, David C. and Hooper, James and Altintas, Bahadir and Zurek, Eva** (2013). Metallization of magnesium polyhydrides under pressure, *Phys. Rev. B*, **87**, 054107.
- [48] **Hermann, Andreas and Ivanov, B. L. and Ashcroft, N. W. and Hoffmann, Roald** (2012). LiBeB: A predicted phase with structural and electronic peculiarities, *Phys. Rev. B*, **86**, 014104.
- [49] **Hooper, James and Baettig, Pio and Zurek, Eva** (2012). Pressure induced structural transitions in KH, RbH, and CsH, *Journal of Applied Physics*, **111**, 112611.
- [50] **Tipton, William W. and Bealing, Clive R. and Mathew, Kiran and Hennig, Richard G.** (2013). Structures, phase stabilities, and electrical potentials of Li-Si battery anode materials, *Phys. Rev. B*, **87**, 184114.
- [51] **William W Tipton and Richard G Hennig** (2013). A grand canonical genetic algorithm for the prediction of multi-component phase diagrams and testing of empirical potentials, *J. Phys.: Condens. Matter*, **25**, 495401.

- [52] **Park, Hyoungki and Feller, Michael R. and Lenosky, Thomas J. and Tipton, William W. and Trinkle, Dallas R. and Rudin, Sven P. and Woodward, Christopher and Wilkins, John W. and Hennig, Richard G.** (2012). Ab initio based empirical potential used to study the mechanical properties of molybdenum, *Phys. Rev. B*, **85**, 214121.
- [53] **Bi, W. and Meng, Y. and Kumar, R. S. and Cornelius, A. L. and Tipton, W. W. and Hennig, R. G. and Zhang, Y. and Chen, C. and Schilling, J. S.** (2011). Pressure-induced structural transitions in europium to 92 GPa, *Phys. Rev. B*, **83**, 104106.
- [54] **Ji Feng, Richard G. Hennig, N. W. Ashcroft & Roald Hoffmann** (2008). Emergent reduction of electronic state dimensionality in dense ordered Li-Be alloys, *Nature*, **451**, 445–448.
- [55] **A. Corana, M. Marchesi, C.M. and Ridella, S.** (September 1987). Minimizing Multimodal Functions of Continuous Variables with the ‘Simulated Annealing’ Algorithm, *ACM Transactions on Mathematical Software*, **13**(3), 262–280.
- [56] **Wolfram Koch, M.C.H.** (2001). *A Chemist’s Guide to Density Functional Theory (Second Edition)*, Oxford University Press.
- [57] **Parr, R.G. and Yang, W.** (1989). *Density-Functional Theory of Atoms and Molecules*, Oxford University Press.
- [58] **Pekka Pyykkö and Michiko Atsumi** (2009). Molecular Double-Bond Covalent Radii for Elements Li–E112, *Chemistry - A European Journal*, **15**, 12770–12779.
- [59] **Pekka Pyykkö and Michiko Atsumi** (2008). Molecular Single-Bond Covalent Radii for Elements 1–118, *Chemistry - A European Journal*, **15**, 186–197.
- [60] **Pekka Pyykkö, Sebastian Riedel and Michael Patzschke** (2005). Triple-Bond Covalent Radii, *Chemistry - A European Journal*, **11**, 3511–3520.
- [61] **B. Hammer, L. B. Hansen, and J. K. Nørskov** (1999). Improved adsorption energetics within density-functional theory using revised Perdew-Burke-Ernzerhof functionals, *Phys. Rev. B*, **59**, 7413.
- [62] **David Vanderbilt** (1990). Soft self-consistent pseudopotentials in a generalized eigenvalue formalism, *Phys. Rev. B*, **41**, 7892.
- [63] **D. F. Shanno** (1970). Conditioning of Quasi-Newton Methods for Function Minimization, *Mathematics of Computation*, **24**, 647–656.
- [64] **Sune R. Bahn and Karsten W. Jacobsen** (2002). An Object-Oriented Scripting Interface to a Legacy Electronic Structure Code, *Comput. Sci. Eng.*, **4**, 56.
- [65] **H. T. Stokes and D. M. Hatch** (2005). FINDSYM: Program for Identifying the Space Group Symmetry of a Crystal., *J. Appl. Cryst.*, **38**, 237–238.
- [66] **Jmol**, An open-source Java viewer for chemical structures in 3D, <http://www.jmol.org/>.

- [67] **K. Momma and F. Izumi** (2011). VESTA 3 for three-dimensional visualization of crystal, volumetric and morphology data, *J. Appl. Cryst.*, **44**, 1272–1276.
- [68] **Varin RA, et al.** (2012). Mechano-chemical synthesis of manganese borohydride ($Mn(BH_4)_2$) and inverse cubic spinel (Li_2MnCl_4) in the ($nLiBH_4 + MnCl_2$) ($n = 1, 2, 3, 5, 9$ and 23) mixtures and their dehydrogenation behavior, *International Journal of Hydrogen Energy*, **37**, 16056–16069.
- [69] **Pabitra Choudhury, V.R.B.E.S.** (2008). Dehydrogenation Thermodynamics of Hydrogen Storage Material Manganese Borohydride: First-Principles Study, *University of South Florida, 4202 E. Fowler Ave., ENB 118, Tampa, FL 33620*.

CURRICULUM VITAE



Name Surname: Engin Aybey

Place and Date of Birth: Uşak, 31/01/1986

B.Sc.: Engineering of Physics, University of Gaziantep, 2005-2010